

Strongly baryon-dominated disk galaxies at the peak of galaxy formation ten billion years ago

R. Genzel^{1,2}, N. M. Förster Schreiber¹, H. Übler¹, P. Lang¹, T. Naab³, R. Bender^{1,4}, L. J. Tacconi¹, E. Wisnioski¹, S. Wuyts^{1,5}, T. Alexander⁶, A. Beifiori^{1,4}, S. Belli¹, G. Brammer⁷, A. Burkert^{1,3}, C. M. Carollo⁸, J. Chan¹, R. Davies¹, M. Fossati^{1,4}, A. Galametz^{1,4}, S. Genel⁹, O. Gerhard¹, D. Lutz¹, J. T. Mendel^{1,4}, I. Momcheva¹⁰, E. J. Nelson^{1,10}, A. Renzini¹¹, R. Saglia^{1,4}, A. Sternberg¹², S. Tacchella⁸, K. Tadaki¹ & D. Wilman^{1,4}

In the cold dark matter cosmology, the baryonic components of galaxies—stars and gas—are thought to be mixed with and embedded in non-baryonic and non-relativistic dark matter, which dominates the total mass of the galaxy and its dark-matter halo¹. In the local (low-redshift) Universe, the mass of dark matter within a galactic disk increases with disk radius, becoming appreciable and then dominant in the outer, baryonic regions of the disks of star-forming galaxies. This results in rotation velocities of the visible matter within the disk that are constant or increasing with disk radius—a hallmark of the dark-matter model². Comparisons between the dynamical mass, inferred from these velocities in rotational equilibrium, and the sum of the stellar and cold-gas mass at the peak epoch of galaxy formation ten billion years ago, inferred from ancillary data, suggest high baryon fractions in the inner, star-forming regions of the disks^{3–6}. Although this implied baryon fraction may be larger than in the local Universe, the systematic uncertainties (owing to the chosen stellar initial-mass function and the calibration of gas masses) render such comparisons inconclusive in terms of the mass of dark matter⁷. Here we report rotation curves (showing rotation velocity as a function of disk radius) for the outer disks of six massive star-forming galaxies, and find that the rotation velocities are not constant, but decrease with radius. We propose that this trend arises because of a combination of two main factors: first, a large fraction of the massive high-redshift galaxy population was strongly baryon-dominated, with dark matter playing a smaller part than in the local Universe; and second, the large velocity dispersion in high-redshift disks introduces a substantial pressure term that leads to a decrease in rotation velocity with increasing radius. The effect of both factors appears to increase with redshift. Qualitatively, the observations suggest that baryons in the early (high-redshift) Universe efficiently condensed at the centres of dark-matter haloes when gas fractions were high and dark matter was less concentrated.

Over the last few years, there have been several important studies of the ionized gas dynamics of star-forming galaxies with redshifts of $z \approx 0.6$ – 2.6 . The galaxies studied were drawn from mass-selected parent samples in cosmological deep fields, and from imaging and grism surveys with the Hubble Space Telescope^{3,5,8–13} with well-characterized properties (see Methods). We obtained deep (5–22-h integration) imaging spectroscopy of the H α emission line with the near-infrared integral field spectrometers SINFONI and KMOS on the Very Large Telescope of the European Southern Observatory as part of our ‘SINS/zC-SINF’ and ‘KMOS^{3D}’ surveys (henceforth ‘IFS samples’^{3,8}). From the data we extract H α rotation curves, and rotation velocities as a

function of galactic radius, for several hundred star-forming galaxies (Methods). Rotation curves provide valuable constraints on the baryonic and dark-matter mass distributions in massive star-forming disks at the peak of cosmic galaxy formation ten billion years ago, and are largely independent of assumptions on star-formation histories and stellar mass functions.

Figure 1 shows the angular distributions of stellar mass and light, integrated H α intensity, H α velocity and dispersion, together with cuts of H α velocity and dispersion along the kinematic major axis, for six star-forming galaxies. From the IFS samples we selected galaxies for deep spectroscopy that have large stellar masses ($\log(M_*/M_\odot) \approx 10.6$ – 11.1 , where M_* and M_\odot are the stellar mass and mass of the Sun, respectively), that have not participated in a merger, that have rotationally dominated kinematics and that have large half-light radii ($R_{1/2} \approx 4$ – 9 kpc), such that the disk penetrates far into the dark-matter halo.

The extracted velocity and velocity dispersion fields in all cases demonstrate that the sources are rotationally supported⁸ (Methods). The ratio of peak rotation velocity v_{rot} to the amplitude of random motions σ_0 , as estimated from the velocity dispersion in the outer disks, is between 4 and 9—lower than in present-day disks ($v_{\text{rot}}/\sigma_0 \approx 10$ – 20) and in excellent agreement with other observations^{3,8}. This difference from the present-day values means that ‘turbulent’ motions contribute substantially to the energy balance¹⁴.

The most surprising result is that the projected rotation velocities along the kinematic major axis (Fig. 1c) reach a maximum value of $|v_{\text{max}}|$ at a radius R_{max} , and decrease for increasing radius R , symmetrically on either side of the galaxy centre. Averaging the two sides of the galaxy improves the signal-to-noise ratio (Fig. 2). The six rotation curves drop to $v_{\text{rot}}(R_{\text{out}})/v_{\text{max}} \approx 0.3$ – 0.9 at the outermost radius sampled, R_{out} . Decreasing, or ‘falling’, rotation curves have previously been detected at low redshift in some compact, high-surface-density or strongly bulged disks (such as Andromeda; Fig. 2), but these are rare and velocity decreases are modest (to $v_{\text{rot}}/v_{\text{max}} \approx 0.8$ – 0.95 ; refs 2, 15–17).

We investigate the prevalence of falling rotation curves at high redshift. A co-added rotation curve¹⁸ of 97 rotationally supported, isolated, $z \approx 0.6$ – 2.6 disks from the same IFS samples that we use (but excluding the six above) provides a representative and fairly unbiased sample of the redshift–stellar mass–star-formation rate parameter space for star-forming galaxies with $\log(M_*/M_\odot) > 9.7$ (see Methods and Extended Data Fig. 1). Star-forming galaxies over the entire mass range of the parent sample enter the stack (Extended Data Fig. 1). Within the uncertainties, the stack confirms the results presented

¹Max-Planck-Institut für extraterrestrische Physik (MPE), Giessenbachstrasse 1, 85748 Garching, Germany. ²Departments of Physics and Astronomy, University of California, Berkeley, California 94720, USA. ³Max-Planck Institute for Astrophysics, Karl Schwarzschildstrasse 1, D-85748 Garching, Germany. ⁴Universitäts-Sternwarte Ludwig-Maximilians-Universität (USM), Scheinerstrasse 1, D-81679 München, Germany. ⁵Department of Physics, University of Bath, Claverton Down, Bath BA2 7AY, UK. ⁶Department of Particle Physics and Astrophysics, Faculty of Physics, The Weizmann Institute of Science, POB 26, Rehovot 76100, Israel. ⁷Space Telescope Science Institute, Baltimore, Maryland 21218, USA. ⁸Institute of Astronomy, Department of Physics, Eidgenössische Technische Hochschule, ETH Zürich, CH-8093 Zürich, Switzerland. ⁹Center for Computational Astrophysics, 160 Fifth Avenue, New York, New York 10010, USA. ¹⁰Department of Astronomy, Yale University, 260 Whitney Avenue, New Haven, Connecticut 06511, USA. ¹¹Osservatorio Astronomico di Padova, Vicolo dell'Osservatorio 5, Padova I-35122, Italy. ¹²School of Physics and Astronomy, Tel Aviv University, Tel Aviv 69978, Israel.

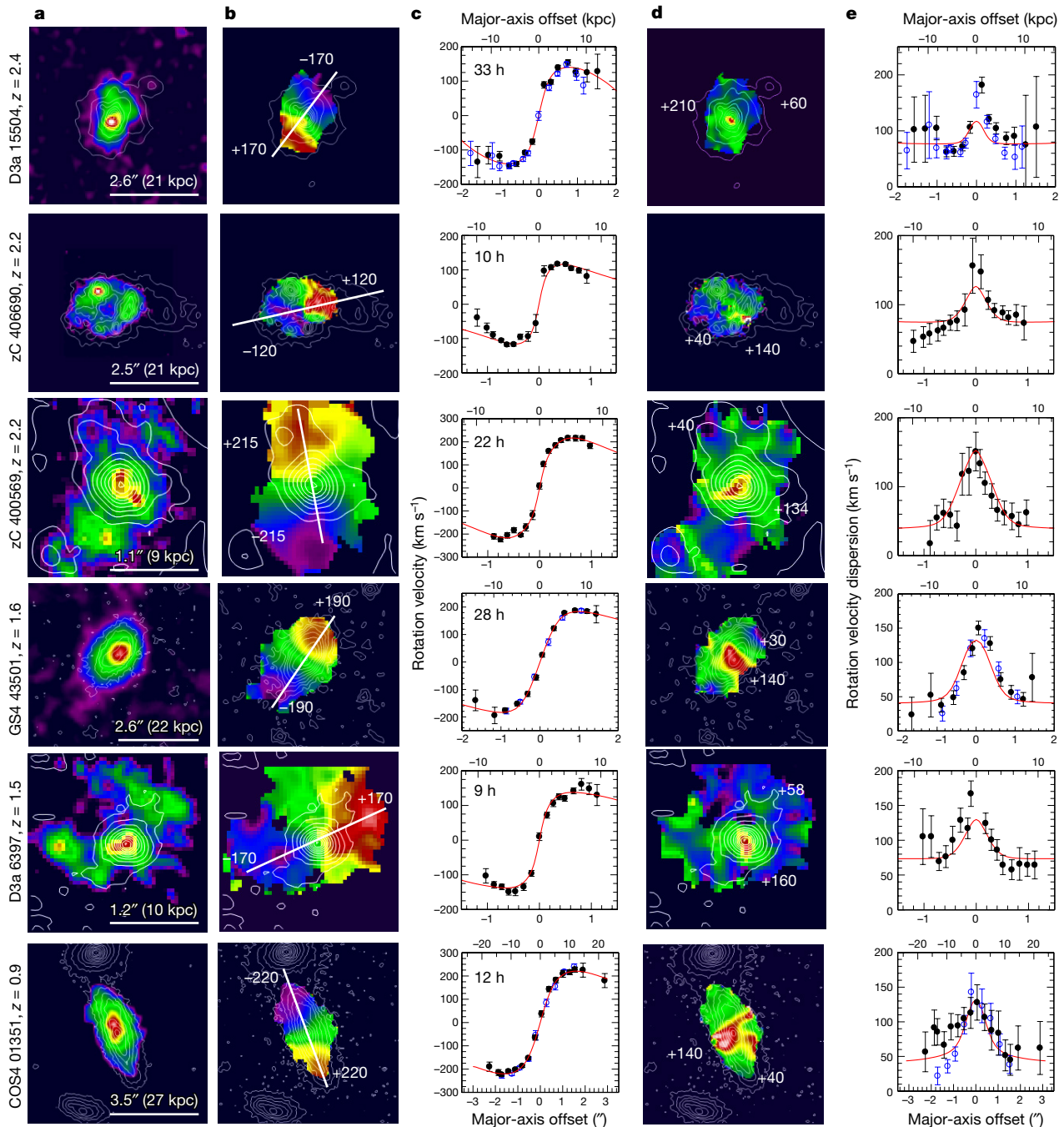


Figure 1 | H α gas dynamics from KMOS and SINFONI in six massive star-forming galaxies. The galaxies have redshifts between $z = 0.9$ and $z = 2.4$. KMOS provides seeing-limited data (full-width at half-maximum, FWHM $\approx 0.6''$); SINFONI allows both seeing-limited and adaptive-optics-assisted observations (FWHM $\approx 0.2''$). **a**, For each galaxy, the distribution of the integrated H α line surface brightness is shown (colour scale; with a linear scaling), superposed on the stellar surface density (Σ_* ; top three panels) or the H-band continuum surface brightness (Σ_H ; bottom three panels) (white contours; square-root scaling). The horizontal white bar denotes the physical size scale. **b**, Velocity maps (colour scale; with extreme values indicated, in km s^{-1}) superposed on Σ_* or Σ_H contours (white lines; square-root scaling), derived from fitting a Gaussian line profile to the H α data in each pixel ($0.05''$). All galaxies have FWHM $\approx 0.25''$ (2 kpc) except GS4 43501 and COS4 01351, which have FWHM $\approx 0.55''$ – $0.67''$ (5 kpc). **c**, Extracted line centroids (and ± 1 r.m.s. uncertainties) along the kinematic major axis (white line in **b**). For COS4 01351 (bottom panel) and GS4 43501 (fourth panel), we show SINFONI (black filled circles) and KMOS (open blue circles) datasets; for D3a 15504 (top panel) we show SINFONI datasets

at $0.2''$ (filled black circles) and $0.5''$ (open blue circles) resolution. Red continuous lines denote the best-fit dynamical model, constructed from a combination of a central compact bulge, an exponential disk and an NFW halo without adiabatic contraction, with a concentration of $c = 4$ at $z \approx 2$ and $c = 6.5$ at $z \approx 1$. For the modelling of the disk rotation, we also take into account the asymmetric drift correction inferred from the velocity dispersion curves (**d** and **e**; ref. 14). The times shown in each panel indicate the total on-source integration time. **d**, **e**, Two-dimensional (**d**; colour scale) and major-axis (**e**; with ± 1 r.m.s. uncertainties) velocity dispersion distributions inferred from the Gaussian fits (after removal of the instrumental response: $\sigma_{\text{instr}} \approx 37 \text{ km s}^{-1}$ at $z \approx 0.85$ and $z \approx 2.2$; $\sigma_{\text{instr}} \approx 45 \text{ km s}^{-1}$ at $z = 1.5$), superposed on Σ_* or Σ_H contours (**d**; white lines). The numbers in **d** indicate the minimum and maximum velocity dispersions. The colouring of the data and red lines in **e** are as in **c**. All physical units are based on a concordance, flat cold dark matter cosmology, with cosmological constant Λ , matter density relative to the critical density of closing the Universe $\Omega_m = 0.3$ and ratio of baryonic to total matter density $\Omega_{\text{baryon}}/\Omega_m = 0.17$, and for the $z = 0$ Hubble parameter $H_0 = 70 \text{ km s}^{-1} \text{ Mpc}^{-1}$.

here for individual sources, and implies that falling rotation curves at $z = 0.6\text{--}2.6$ are common. The uncertainties of individual velocity measurements in the faint outer disks are substantial, such that the significance of the velocity decreases in each individual data point is at most 3.5 times the root-mean-square (r.m.s.). When all data points corresponding to radii greater than R_{max} are considered together, the statistical significance for a non-flat, falling rotation curve becomes compelling (6–10 r.m.s.).

We investigated the possibility that the falling rotation curves are artefacts, caused by warping of the disks, radial streaming along galactic bars, radial changes in the direction of the kinematic axis, tidal interactions with nearby satellites, or non-equilibrium motions caused by variations in the amount or direction of the baryonic accretion (Methods). We find interacting low-mass satellites in three of our six sources, and evidence for some tidal stripping in one, but the rotation curve for this source is symmetric, even near the satellite. We also see strong radial streaming confined to the nuclear region in one galaxy. Warps are expected because of the non-planar accretion of gas from the intergalactic web, but are also less likely to be stable at high redshift than in the low-redshift Universe, because of the large, isotropic velocity dispersions. The point-symmetric, falling rotation curves in Fig. 1 argue against strong warping. We also find no evidence in the two-dimensional residual maps (data minus model) for radial variations in the line of nodes, as a result of interactions and variations in the angular momentum of the incoming gas (Extended Data Fig. 6). Four galaxies have massive bulges (ratio of the mass of the bulge to that of the total galaxy, $B/T > 0.3$), which will probably accentuate centrally peaked rotation curves. Keeping in mind the important effects of non-equilibrium dynamics in the early phases of galaxy formation, the prevalence of point-symmetric, smooth rotation curves in all six cases suggests that these are intrinsic properties of the galaxies.

We compare the final average of all seven rotation curves with an average rotation curve for local massive disks¹⁹, the curves for the Milky Way²⁰ and M31¹⁷, and the theoretical curve for a thin, purely baryonic, exponential ‘Freeman’ disk²¹ (Fig. 2b). All of the local rotation curves lie above the Freeman model, and so require additional (dark) matter in various amounts. In contrast, the average curve for high-redshift disks is consistent with the curve for a pure baryonic disk to $R \approx 1.8R_{1/2}$, and falls below it for larger R .

Because high-redshift disks exhibit large random motions, the equation of hydrostatic equilibrium of the disk contains a radial pressure gradient, which slows down the rotation velocity (‘asymmetric drift’¹⁴; Methods). If we apply this correction and also allow for the resultant large thickness of the disk, then the rotation curve indeed drops rapidly with radius, as long as σ_0 stays approximately constant. Figure 2 shows data for a galaxy with $v_{\text{rot}}/\sigma_0 \approx 5$, demonstrating excellent agreement with the average observations.

Our analysis only allows for a small contribution of dark matter in the mass budget of the outer disks (and inner haloes) of massive, high-redshift star-forming galaxies. This conclusion is consistent with the earlier, but less conclusive (owing to uncertainties in the stellar initial-mass function, the star formation history and the gas masses), analysis of the inner-disk dynamics^{3–6} (Methods). We quantify our conclusion by fitting the major-axis velocity and velocity dispersion data for each galaxy (Fig. 1) with a three-component mass model, which consists of the sum of a central compact (spheroidal) stellar bulge, an exponential gaseous and stellar disk, and a Navarro–Frenk–White (NFW) dark-matter halo²². The output of the fitting is the fraction of the total mass that corresponds to dark matter at $R_{1/2}$, $f_{\text{DM}}(R = R_{1/2})$ (Methods). We list the fitting results (and ± 2 r.m.s. uncertainties) in Table 1 and summarize them in Fig. 3, in which the high-redshift data is compared to previous low-redshift results⁷ and to the results of ref. 6. With these basic assumptions, we find that the dark-matter fractions near the half-light radius $R_{1/2}$ for all of the galaxies we studied are modest to negligible, even when the various parameter correlations and uncertainties are included (Fig. 3 and Methods). We note

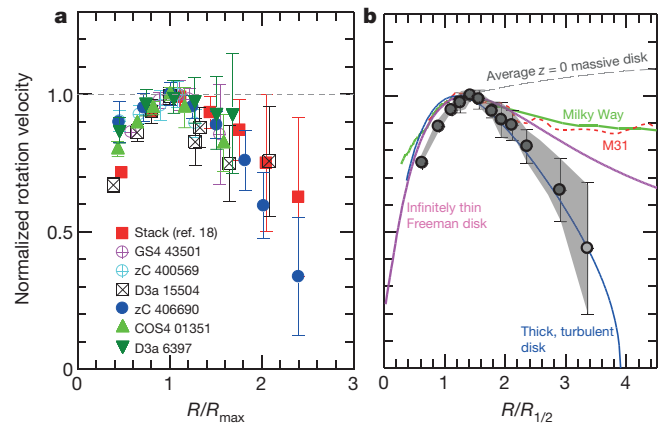


Figure 2 | Normalized rotation curves. **a**, The various symbols denote the folded and binned rotation curve data for the six galaxies in Fig. 1, combined with the stacked rotation curve of 97 $z = 0.6\text{--}2.6$ star-forming galaxies¹⁸ (Methods). For all rotation curves, we averaged data points located symmetrically on either side of the dynamical centres, and plot the rotation velocities normalized by the maximum rotation velocity against the radii R normalized by the radius at which the amplitude of the rotation velocity is maximum ($|v_{\text{rot}}| = v_{\text{max}}$), R_{max} . Error bars are ± 1 r.m.s. **b**, The black data denote the binned averages of the six individual galaxies, as well as the stack shown in **a**, with 1 r.m.s. uncertainties of the error-weighted means shown as grey shading (the outermost point has lighter shading to indicate that only two data points entered the average). In individual galaxies, R_{max} depends on the ratio of bulge to total baryonic mass of the galaxy, the size of the galaxy and the instrumental resolution, leading to varying amounts of beam smearing. We assume an average value of $R_{\text{max}} \approx (1.3\text{--}1.5)R_{1/2}$. For comparison, the grey dashed line indicates the slope of a typical rotation curve for low-redshift ($z = 0$), massive ($\log(M_*/M_\odot) \approx 11$), star-forming disk galaxies¹⁹, which are comparable to the six galaxies we studied; the dotted red and solid green curves are the rotation curves of M31 (the Andromeda galaxy)¹⁷ and the Milky Way²⁰. The thick magenta curve is the rotation curve of an infinitely thin, ‘Freeman’ exponential disk²¹ with Sérsic index $n_{\text{Sérsic}} = 1$. The blue curve is a turbulent, thick exponential disk, including ‘asymmetric drift’ corrections for an assumed radially constant velocity dispersion of $\sigma_0 \approx 50 \text{ km s}^{-1}$ (and a ratio of rotation velocity to dispersion of $v_{\text{rot}}/\sigma_0 \approx 5$)¹⁷.

that spatially variable σ_0 and deviations from planarity and exponential disk distributions undoubtedly make reality more complex than can be captured in these simple models.

All six disks that we study are ‘maximal’⁷ ($f_{\text{DM}} < 0.28$). Their dark-matter fractions are at the lower tail of local star-forming disks, and in the same region of v_c – f_{DM} parameter space as local massive, passive galaxies²³ and some strongly bulged, early-type disks⁷, where the circular velocity v_c is defined in equation (1) in Methods. Dark-matter fractions decrease as redshift increases from 0.8 to 2.3 (ref. 6; Table 1, Fig. 3). The agreement between the dark-matter fractions in the $z = 0.6\text{--}2.6$ star-forming galaxies and in local passive galaxies is interesting. Passive galaxies are probably the descendants of the massive main-sequence star-forming population that we observe in our IFS samples. Star formation in these galaxies was probably rapidly quenched at $z \leq 2$ once they had grown to masses comparable to the galaxy mass function characteristic Schechter mass, $M_{\text{Schechter}} \approx 10^{10.6\text{--}10.9} M_\odot$, after which they transitioned to the passive galaxy sequence²⁴. The low dark-matter fractions in the high-redshift star-forming galaxies may therefore be preserved in the properties of the local passive population.

There are several reasons for why high-redshift disks should be more baryon-dominated than low-redshift disks. First, high-redshift disks are gas rich and compact. Star-forming galaxies at $z \approx 2.3$ have molecular-gas-to-stellar-mass ratios about 25 times larger than those of $z = 0$ galaxies²⁵ ($M_{\text{molgas}}/M_* \propto (1+z)^{2.7}$), are 2.4 times smaller in size²⁶ ($R_{1/2} \propto (1+z)^{-0.75}$), and so have molecular gas surface densities that are more than two orders of magnitude greater than those of local

Table 1 | Physical parameters of observed star-forming galaxies

	COS4 01351	D3a 6397	GS4 43501	zC 406690	zC 400569	D3a 15504
Redshift, z	0.854	1.500	1.613	2.196	2.242	2.383
Scale (kpc arcsec ⁻¹)	7.68	8.46	8.47	8.26	8.23	8.14
Priors						
Stellar mass, M_* ($10^{11}M_\odot$)	0.54 ± 0.16	1.2 ± 0.37	0.41 ± 0.12	0.42 ± 0.12	1.2 ± 0.37	1.1 ± 0.34
Total (gas + stars) baryonic mass, M_{baryon} ($10^{11}M_\odot$)	0.9 ± 0.5	2.3 ± 1.1	0.75 ± 0.37	1.4 ± 0.7	2.5 ± 1.2	2.0 ± 1.0
H-band half-light radius, $R_{1/2}$ (kpc)	8.6 ± 1.3	5.9 ± 0.8	4.9 ± 0.7	5.5 ± 1	4 ± 2	6.3 ± 1
Inclination, i (°)	75 ± 5	30 ± 5	62 ± 5	25 ± 12	45 ± 10	34 ± 5
Dark-matter concentration parameter, c	6.8	5	5	4	4	4
Fit parameters						
$v_c(R=R_{1/2})^*$ (km s ⁻¹)	276	310	257	301	364	299
$R_{1/2}(n=1)$ (kpc)	7.3	7.4	4.9	5.5	3.3	6
Velocity dispersion, σ_0 (km s ⁻¹)	39	73	39	74	34	76
Total (gas + stars, including bulge) baryonic mass, M_{baryon} ($10^{11}M_\odot$)	1.7	2.3	1.0	1.7	1.7	2.1
$M_{\text{bulge}}/M_{\text{baryon}}^\dagger$	0.2	0.35	0.4	0.6	0.37	0.15
$f_{\text{DM}}(R=R_{1/2})^\ddagger$	0.21 (0.1)	0.17 (<0.38)	0.19 (0.09)	0.0 (<0.08)	0.0 (<0.07)	0.12 (<0.26)

*Total circular velocity at the half-light radius (rest-frame optical) $R_{1/2}$, including bulge, exponential disk ($n=1$) and dark matter, and corrected for asymmetric drift:

$$v_c(R)^2 = v_{\text{rot}}(R)^2 + 3.36\sigma_0^2(R/R_{1/2})|_{n=1}.$$

$^\dagger M_{\text{bulge}}$ is the baryonic mass confined to the central 1 kpc of the galaxy, less the contribution from the exponential disk.

‡ Ratio of dark-matter mass to total mass at the best-fit half-light radius of the optical light, $f_{\text{DM}}(R=R_{1/2}) = (v_{\text{DM}}/v_c)^2|_{R=R_{1/2}}$; numbers in parentheses are the ± 2 r.m.s. or upper limits (goodness of fit $\chi^2=4$, about 95% probability) uncertainties. We use an NFW halo with concentration parameter c and no adiabatic contraction.

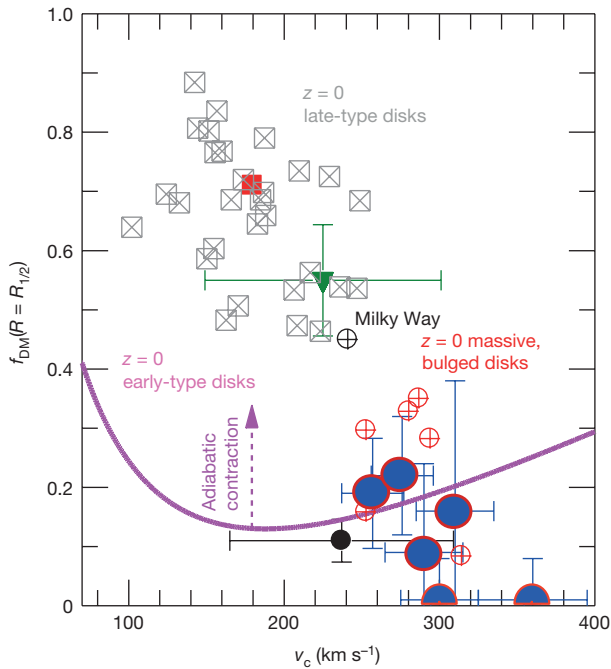


Figure 3 | Dark-matter fractions. Dark-matter fractions f_{DM} from different methods are listed as a function of the circular velocity of the disk v_c , at approximately the half-light radius of the disk $R_{1/2}$, for galaxies in the current Universe and about 10 Gyr ago. The large blue circles with red outlines indicate the dark-matter fractions derived from the outer-disk rotation curves for the six high-redshift disks presented here (Table 1), along with the ± 2 r.m.s. uncertainties of the inferred dark-matter fractions and circular velocities. The average dark-matter fractions (and their ± 1 r.m.s. errors/dispersions in the two coordinates) obtained from the comparison of inner rotation curves and the sum of stellar and gas masses for 92 $z=2-2.6$ and 106 $z=0.6-1.1$ star-forming galaxies are indicated by the filled black circle and green triangle, respectively⁶. We compare these high-redshift results to $z=0$ estimates obtained using different independent techniques for late-type, star-forming disks⁷ (crossed grey squares, red filled square), for the Milky Way²⁰ (crossed black circle), for massive, bulged, lensed disks⁷ (crossed red circles), and for passive early-type disks²³ (thick magenta line). The upward magenta arrow marks the typical change if the $z=0$ data dark-matter haloes are maximally adiabatically contracted.

galaxies. Large gas columns can easily dissipate angular momentum and drive gas inward. The strong redshift dependence of the gas fractions could explain the decrease in f_{DM} between $z=2.3$ and $z=1$ (Fig. 3). Second, massive galaxies at high redshift are thought to grow by rapid gas accretion, gas-rich mergers and star formation triggered by this accretion^{27,28}. In this dissipation-dominated peak phase of galaxy growth, the centres of dark-matter haloes can become baryon-dominated in ‘compaction events’ that are triggered by mergers, disk instabilities or colliding streams in the intergalactic web²⁹, or by gas ‘pile-up’ at early times when the gas accretion rates were larger than the star formation consumption rates. However, results from abundance matching indicate that the average stellar-to-dark-matter ratio at the virial radius of the halo does not depend strongly on cosmic epoch and is well below the cosmic baryon fraction $f_b \approx 0.17$, suggestive of very efficient removal of baryons by galactic outflows³⁰.

Third, it is also possible that the baryon dominance is caused by a lack of dark matter in the inner disk. These dark-matter haloes could deviate from the standard NFW profile, with low concentration parameter ($c < 5$), if they were still growing rapidly and not yet in equilibrium, or if they were perturbed by strong stellar and active-galactic-nucleus feedback. We discuss some of these alternatives, such as low concentration parameters, and provide a quantitative comparison between observations and simulations in Methods.

Online Content Methods, along with any additional Extended Data display items and Source Data, are available in the online version of the paper; references unique to these sections appear only in the online paper.

Received 13 November 2016; accepted 31 January 2017.

- White, S. D. M. & Rees, M. J. Core condensation in heavy halos: a two-stage theory for galaxy formation and clustering. *Mon. Not. R. Astron. Soc.* **183**, 341–358 (1978).
- Sofue, Y. & Rubin, V. Rotation curves of spiral galaxies. *Annu. Rev. Astron. Astrophys.* **39**, 137–174 (2001).
- Förster Schreiber, N. M. *et al.* The SINS survey: SINFONI integral field spectroscopy of $z \sim 2$ star-forming galaxies. *Astrophys. J.* **706**, 1364–1428 (2009).
- van Dokkum, P. G. *et al.* Forming compact massive galaxies. *Astrophys. J.* **813**, 23 (2015).
- Price, S. H. *et al.* The MOSDEF survey: dynamical and baryonic masses and kinematic structures of star-forming galaxies at $1.4 \leq z \leq 2.6$. *Astrophys. J.* **819**, 80 (2016).
- Wuyts, S. *et al.* KMOS^{3D}: dynamical constraints on the mass budget in early star-forming disks. *Astrophys. J.* **831**, 149 (2016).
- Courteau, S. & Dutton, A. A. On the global mass distribution in disk galaxies. *Astrophys. J.* **801**, L20 (2015).

8. Wisnioski, E. *et al.* The KMOS^{3D} survey: design, first results, and the evolution of galaxy kinematics from $0.7 \leq z \leq 2.7$. *Astrophys. J.* **799**, 209 (2015).
9. Grogan, N. A. *et al.* CANDELS: the Cosmic Assembly Near-infrared Deep Extragalactic Legacy Survey. *Astrophys. J. Suppl. Ser.* **197**, 35 (2011).
10. Koekemoer, A. M. *et al.* CANDELS: the Cosmic Assembly Near-infrared Deep Extragalactic Legacy Survey—the *Hubble Space Telescope* observations, imaging data products, and mosaics. *Astrophys. J. Suppl. Ser.* **197**, 36 (2011).
11. Kong, X. *et al.* A wide area survey for high-redshift massive galaxies. I. Number counts and clustering of BzKs and EROs. *Astrophys. J.* **638**, 72–87 (2006).
12. Brammer, G. B. *et al.* 3D-HST: a wide-field grism spectroscopic survey with the *Hubble Space Telescope*. *Astrophys. J. Suppl. Ser.* **200**, 13 (2012).
13. Momcheva, I. G. *et al.* The 3D-HST survey: *Hubble Space Telescope* WFC3/G141 grism spectra, redshifts, and emission line measurements for $\sim 100,000$ galaxies. *Astrophys. J. Suppl. Ser.* **225**, 27 (2016).
14. Burkert, A. *et al.* High-redshift star-forming galaxies: angular momentum and baryon fraction, turbulent pressure effects, and the origin of turbulence. *Astrophys. J.* **725**, 2324–2332 (2010).
15. Casertano, S. & van Gorkom, J. H. Declining rotation curves: the end of a conspiracy? *Astron. J.* **101**, 1231–1241 (1991).
16. Honma, M. & Sofue, Y. On the Keplerian rotation curves of galaxies. *Publ. Astron. Soc. Jap.* **49**, 539–545 (1997).
17. Carignan, C., Chemin, L., Huchtmeier, W. K. & Lockman, F. J. The extended H I rotation curve and mass distribution of M31. *Astrophys. J.* **641**, L109–L112 (2006).
18. Lang, P. *et al.* Falling outer rotation curves of star-forming galaxies at $0.6 \leq z \leq 2.6$ probed with KMOS^{3D} and SINS/zC-SINF (submitted).
19. Catinella, B., Giovanelli, R. & Haynes, M. P. Template rotation curves for disk galaxies. *Astrophys. J.* **640**, 751–761 (2006).
20. Bland-Hawthorn, J. & Gerhard, O. The galaxy in context: structural, kinematic, and integrated properties. *Annu. Rev. Astron. Astrophys.* **54**, 529–596 (2016).
21. Freeman, K. On the disks of spiral and S0 galaxies. *Astrophys. J.* **160**, 811–830 (1970).
22. Navarro, J. F., Frenk, C. S. & White, S. D. M. A universal density profile from hierarchical clustering. *Astrophys. J.* **490**, 493–508 (1997).
23. Cappellari, M. *et al.* The ATLAS^{3D} project – XV. Benchmark for early-type galaxies scaling relations from 260 dynamical models: mass-to-light ratio, dark matter, fundamental plane and mass plane. *Mon. Not. R. Astron. Soc.* **432**, 1709–1741 (2013).
24. Peng, Y. *et al.* Mass and environment as drivers of galaxy evolution in SDSS and zCOSMOS and the origin of the Schechter function. *Astrophys. J.* **721**, 193–221 (2010).
25. Genzel, R. *et al.* Combined CO and dust scaling relations of depletion time and molecular gas fractions with cosmic time, specific star-formation rate, and stellar mass. *Astrophys. J.* **800**, 20 (2015).
26. van der Wel, A. *et al.* 3D-HST+CANDELS: the evolution of the galaxy size-mass distribution since $z = 3$. *Astrophys. J.* **788**, 28 (2014).
27. Guo, Q. & White, S. D. M. Galaxy growth in the concordance Λ CDM cosmology. *Mon. Not. R. Astron. Soc.* **384**, 2–10 (2008).
28. Oser, L., Ostriker, J. P., Naab, T., Johansson, P. H. & Burkert, A. The two phases of galaxy formation. *Astrophys. J.* **725**, 2312–2323 (2010).
29. Zolotov, A. *et al.* Compaction and quenching of high- z galaxies in cosmological simulations: blue and red nuggets. *Mon. Not. R. Astron. Soc.* **450**, 2327–2353 (2015).
30. Moster, B. P., Naab, T. & White, S. D. M. Galactic star formation and accretion histories from matching galaxies to dark matter haloes. *Mon. Not. R. Astron. Soc.* **428**, 3121–3138 (2013).

Acknowledgements We thank our colleagues at ESO-Garching and ESO-Paranal, as well as those in the 3D-HST and SINFONI/zC-SINF and KMOS/KMOS^{3D} teams, for their support and high-quality work, which made these technically difficult observations possible. D.W. and M.F. acknowledge the support provided by DFG Projects WI 3871/1-1 and WI 3871/1-2. J.C. acknowledges the support of the Deutsche Zentrum für Luft- und Raumfahrt (DLR) via Project ID 500R1513. T.A. and A.S. acknowledge support by the I-CORE Program of the PBC and Israel Science Foundation (Center No. 1829/12). We thank S. Lilly and A. Dekel for comments on the manuscript. This work is based on observations obtained at the Very Large Telescope (VLT) of the European Southern Observatory (ESO), Paranal, Chile (ESO programme IDs 076.A-0527, 079.A-0341, 080.A-0330, 080.A-0635, 082.A-0396, 183.A0781, 091.A-0126, 092.A-0091, 093.A-0079, 094.A-0217, 095.A-0047, 096.A-0025, 097.B-0065 and 097.A-0353).

Author Contributions Drafting text, figures and Methods: R.G., N.M.F.S., H.Ü., T.N., L.J.T., O.G., D.L., A.R., R.S. and A.S.; data analysis and modelling: R.G., H.Ü., P.L., S.W. and R.D.; data acquisition and reduction: R.G., N.M.F.S., H.Ü., P.L., L.J.T., E.W., S.W., A.Be., S.B., J.C., M.F., A.G., J.T.M. and K.T.; KMOS^{3D} and SINS/zC-SINF IFS survey design and management: N.M.F.S., R.B., E.W., C.M.C., A.R., R.S., S.T. and D.W.; 3D-HST survey analysis: N.M.F.S., S.W., G.B., I.M. and E.J.N.; theoretical interpretation: T.N., T.A., A.Bu., S.G. and O.G.

Author Information Reprints and permissions information is available at www.nature.com/reprints. The authors declare no competing financial interests. Readers are welcome to comment on the online version of the paper. Publisher's note: Springer Nature remains neutral with regard to jurisdictional claims in published maps and institutional affiliations. Correspondence and requests for materials should be addressed to R.G. (genzel@mpe.mpg.de) or N.M.F.S. (forster@mpe.mpg.de).

METHODS

Galaxy samples. The galaxies discussed in this paper were taken from two near-infrared integral field spectroscopic samples ('IFS samples') of distant, massive ($\log(M_*/M_\odot) \gtrsim 9.6$) star-forming galaxies, targeting primarily rest-frame optical emission around the H α line:

(1) the SINS/zC-SINF survey of $z \approx 1.5$ – 2.5 star-forming galaxies^{3,31} observed with SINFONI on the ESO Very Large Telescope^{32,33} (VLT) in both seeing-limited mode ($2R_{1/2,\text{beam}} = \text{FWHM} \approx 0.45''$ – $0.6''$) and at higher resolution with adaptive optics (AO; $\text{FWHM} \approx 0.15''$ – $0.25''$); and

(2) the first 2.5-year sample from the ongoing five-year KMOS^{3D} survey of $0.6 < z < 2.6$ galaxies⁸, all observed in seeing-limited mode ($\text{FWHM} \approx 0.4''$ – $0.7''$) with the KMOS multiplexed IFS instrument on the VLT³⁴.

The IFS sample galaxies are bench-marked to be representative in all important physical parameters of the high-redshift, 'field' star-forming population (stellar mass, star formation rate and size). We have not included galaxies in very dense ('cluster'-like) environments, and mergers or strongly interacting galaxies are relatively rare⁸. These galaxies are located on and around (± 0.6 dex) of the 'star-formation main sequence' at all redshifts included. Below, we summarize the selection criteria used for drawing the individual objects and the stacking sample from the SINS/zC-SINF and KMOS^{3D} surveys, and discuss how their stellar, structural and kinematic properties were derived. A comprehensive description of the surveys, target selections and galaxy properties can be found in refs 9, 10, 12, 13, 36 and 38.

Outer rotation curve samples. The six individual galaxies studied here were selected for very sensitive follow-up observations primarily on the basis of their having (i) high-quality and high-signal-to-noise data in the initial SINFONI and KMOS observations, (ii) rotation-dominated disk kinematics from H α , with a ratio of rotation velocity to velocity dispersion of $v_{\text{rot}}/\sigma_0 > 3$, (iii) no bright neighbouring galaxy in line or continuum emission, and (iv) extended well-resolved star-forming disks. All six galaxies lie close to the main-sequence of star-forming galaxies at $\log(M_*/M_\odot) \geq 10.5$. By design, their half-light radii ($R_{1/2} \gtrsim 4$ kpc) place them in the upper half of the size distribution of massive star-forming galaxies, such that their disk emission probes further into the halo than for typical star-forming galaxies, and such that their inferred baryonic angular momenta are comparable to or larger than the population average³⁵ (about 0.037). Smaller galaxies would therefore place less stringent constraints on the dark-matter fraction in the outer disk, although they are likely to be even more baryon-dominated⁴. Although an optimum selection of rotation-curve candidates would favour high-inclination galaxies, the six galaxies exhibit a wide range of inclinations ($i \approx 25^\circ$ – 75°), with the low inclination systems drawn from the AO SINS/zC-SINF sample (N.M.F.S. *et al.*, manuscript in preparation), which is high quality in terms of angular resolution and depth, but too small to allow an inclination cut.

For the stacking analysis¹⁸, we selected star-forming galaxies on the basis of their SINFONI or KMOS H α kinematics and their Hubble Space Telescope (HST) rest-optical morphologies as follows: (i) rotation-dominated disk kinematics from H α with $v_{\text{rot}}/\sigma_0 > 1$, and (ii) detection of a substantial change of slope in the extracted velocity curve. The latter criterion is the most stringent one: although roughly 3/4 of the parent KMOS^{3D} and SINS/zC-SINF samples are fairly unperturbed, rotation-dominated disks, only half of these show a flattening of the velocity curve at large radii. This large downsizing from the initial samples is driven by the limited field of view (FOV) of the IFS data not reaching the radius of velocity turnover for the more extended galaxies (about $3'' \times 3''$ for the KMOS IFS samples with which the largest parent sample was observed and for the AO-assisted SINFONI data with a scale of $0.05''$ per pixel, and about $4'' \times 4''$ for the seeing-limited SINFONI data at $0.125''$ per pixel with the on-source dithering strategy used for most targets), or by insufficient signal-to-noise at large radii to detect a change of slope. The resultant stacking sample consists of 103 near-main-sequence galaxies spanning $0.6 \leq z \leq 2.6$ and $9.3 \leq \log(M_*/M_\odot) \leq 11.5$. Their size and angular-momentum distributions overlap well with those of the bulk of star-forming galaxies in similar redshift and mass ranges; there is only a mild bias towards larger $R_{1/2}$ for galaxies entering the stack, especially for the $z > 1.3$ subset, which is caused primarily by the implicit signal-to-noise requirement at large radii imposed by the necessity of detecting the flattening of a velocity curve. We performed simulations to determine that the selection criteria and analysis methodology (see below) did not introduce a substantial bias in the shape of the resulting stacked rotation curve. A more detailed discussion of the stacking methodology and so on is provided below.

We compare the distributions in stellar mass, star-formation rate and size properties of the six individual galaxies, the stacking sample, and the parent SINS/zC-SINF and KMOS^{3D} samples to those of the underlying $\log(M_*/M_\odot) \geq 9.0$ galaxy population drawn from the 3D-HST survey source catalogue at $J_{\text{HAB}} < 26$ mag (for which the mass completeness is below $\log(M_*/M_\odot) = 9.0$ out to $z = 3$)^{13,36} in the five CANDELS extragalactic fields^{9,10} (Extended Data Fig. 1). To account for the

large evolution in star-formation rate and size at fixed mass, Extended Data Fig. 1 shows the offsets in star-formation rate relative to the main sequence at the same z and M_* (ref. 37), and the offsets in effective radius at rest-frame $5,000 \text{ \AA}$ relative to the mass–size relation for star-forming galaxies²⁶.

Parent kinematic samples. The SINS/zC-SINF H α sample was drawn from large optical spectroscopic surveys of high-redshift candidates photometrically pre-selected in multi-band imaging surveys on the basis of various magnitude and colour criteria at optical-to-mid-infrared wavelengths. As extensively described^{3,31}, the SINS/zC-SINF H α sample collectively provides a reasonable representation of massive star-forming galaxies at $z \approx 1.5$ – 2.5 , with some bias towards bluer systems stemming from the primary criterion of having a secure optical spectroscopic redshift. In addition, the objects chosen for the near-infrared SINFONI observations were required to have H α falling away from bright OH sky lines and within high atmospheric transmission windows, and to have an expected total H α flux of more than about $5 \times 10^{-17} \text{ erg s}^{-1} \text{ cm}^{-2}$ or, correspondingly, a star-formation rate of more than about $10 M_\odot \text{ yr}^{-1}$ assuming a typical visual extinction of $A_V \approx 1$ mag. The latter flux criterion was applied last and did not greatly affect the final set of targets.

The KMOS^{3D} sample was taken from the '3D-HST' source catalogue^{12,13,36} in fields with deep HST imaging from the CANDELS Treasury programme^{9,10} and $R \approx 130 \lambda = 1.1$ – $1.7 \mu\text{m}$ slitless spectroscopy using the HST WFC3/G141 grism from the 3D-HST Treasury programme³⁸. Multi-band photometry and grism spectra were extracted for sources reaching $J_{\text{HAB}} \approx 26$ mag; redshifts were determined from the grism spectra (probing Balmer/4,000-Å continuum break and/or emission lines) combined with the full optical-to-mid-infrared photometry and supplemented with spectroscopic redshifts available from the literature^{13,36}. The KMOS^{3D} targets were selected primarily to have a stellar mass of more than about $10^{9.5} M_\odot$ (derived from modelling the photometry; see below) and $K_{\text{AB}} = 23$ mag, and a sufficiently accurate redshift (dominated by grism and spectroscopic redshifts) ensuring avoidance of sky lines and poor telluric transmission for H α . No explicit cut in star-formation rate, colour or size was applied. Both the 3D-HST and KMOS^{3D} near-infrared and mass selections result in a wide coverage of the full underlying galaxy population $0.7 < z < 2.7$, including the redder dust-obscured and/or more massive objects. In the first 2.5 years of our on-going KMOS^{3D} survey, we emphasized high-mass targets (but over a very wide range of three orders of magnitude in specific star-formation rate relative to the 'main-sequence' relationship). The resultant mass distribution is weighted towards high masses compared to a purely mass-selected sample; however, once accounting for this bias, the sample provides a good representation of the underlying galaxy population in other properties^{6,8,35}.

Global stellar and gas properties. The global stellar properties were derived following the procedures outlined in ref. 39. In brief, stellar masses were obtained from fitting the observed broadband optical-to-near-/mid-infrared (rest-ultraviolet to optical/near-infrared) spectral energy distributions (SEDs) with population synthesis models⁴⁰, adopting a reddening law⁴¹, an initial mass function⁴², a solar metallicity and a range of star-formation histories (constant star-formation rate or exponentially declining or increasing star-formation rates with varying e-folding timescales). Over the mass and redshift ranges of the galaxies, gas-phase O/H abundances inferred from rest-optical nebular emission lines suggest metallicities of about 1/4 to 1 times the metallicity of the Sun^{43–50}. Varying the assumed metallicity in this range would change the stellar masses in our modelling by less than 0.1 dex (refs 3, 51). Given this small effect and the uncertainties in metallicity determinations for high-redshift star-forming galaxies⁵², we chose to keep a fixed solar metallicity. Note that here we define stellar mass as the 'observed' mass ('live' stars plus remnants), after mass loss from stars.

The star formation rates were obtained from rest-frame ultraviolet + infrared luminosities through the Herschel–Spitzer-calibrated ladder of star-formation-rate indicators³⁹ or, if infrared luminosities are not available (from lack of observations or the source was undetected), from the broadband SED modelling described above.

Individual determinations of molecular gas masses (from CO line or submillimetre/far-infrared dust continuum emission) are scarce for our galaxy samples, and atomic hydrogen masses are not known for any of our high-redshift star-forming galaxies. We computed molecular gas masses from the general scaling relations between star-formation rates, stellar masses and molecular gas masses for main-sequence galaxies (as a function of redshift)^{25,53}. We assumed, as argued previously²⁵, that at $z \approx 1$ – 3 the cold gas content of star-forming galaxies is dominated by the molecular component such that the atomic fraction can be neglected. As such, the gas masses estimated from these scaling relations may be lower limits.

Structural properties. The stellar structural parameters used as priors in our detailed kinematic modelling were derived by fitting two-dimensional Sérsic models to the high-resolution H-band images from HST observations available for all KMOS^{3D} objects and most SINS/zC-SINF galaxies^{6,26,54–59}. For the remainder of the SINS/zC-SINF galaxies (without HST imaging), structural parameters were

estimated from the line integrated H α distributions and/or from the continuum images synthesized from the IFS sample data, depending on the galaxy. To first order, this approach is justified because high-redshift star-forming galaxies are gas-rich, with large star-formation rates and young stellar populations; however, there are some small systematic differences on average because of the presence of substantial stellar bulges in the more massive star-forming galaxies and of possible bright clumps and asymmetric distributions in tracers of on-going star formation^{57,60–64}. Of the individual galaxies and stacking sample of interest here, only D3a 6397 lacks HST imaging.

For all but the most massive $z \approx 1$ –3 star-forming galaxies, the stellar and H α surface-brightness distributions of main-sequence galaxies across the mass and redshift range discussed here are reasonably well fitted by near-exponential (Sérsic index $n_{\text{Sérsic}} \approx 1$ –1.5) profiles^{57,61,63–68} (see also N.M.F.S. *et al.*, manuscript in preparation). Above $\log(M_*/M_\odot) \approx 11$, $z \approx 1$ –3 star-forming galaxies feature a prominent stellar bulge component with characteristic $R_{1/2} \approx 1$ kpc and median bulge-to-total ratio in H-band light reaching about 20%–30% (and higher, about 40%–50%, in terms of stellar mass ratio^{57,63,64}). Although central drops in H α equivalent width, and even flux, of individual galaxies appear to be more frequent at the high-mass end, there is evidence that on average the profiles are near-exponential⁶⁹ and that otherwise large central gas and dust concentrations may be present and obscure the optical light from star-forming regions in the inner parts of massive star-forming galaxies^{62,70–72}. These findings motivate our modelling assumption that the baryonic component is distributed in a compact spheroidal bulge at the centre of an exponential disk.

The estimates of half-light (effective) radii $R_{1/2}$ used for the galaxies refer to the major-axis radii. To determine the inclination from the best-fit axial ratios, we account for the fact that for the mass range $\log(M_*/M_\odot) > 10$ spanned by most galaxies of interest here, half or more of the high-redshift star-forming galaxies consist of symmetric, oblate thick disks^{73–75}, linked to their large intrinsic gas velocity dispersion^{3,8,76–79} and $v_{\text{rot}}/\sigma_0 \lesssim 10$. We note that the H band probes a large range of rest-frame wavelengths over the $0.6 < z < 2.6$ redshift range of the individual galaxies and stacked sample considered here. A ‘k-correction’²⁶ should ideally be applied to the structural parameters for consistency (and similarly, a statistical correction between H α and rest-optical sizes could be applied)⁶⁹. However, the uncertainties adopted for the size and inclination priors are larger than these corrections would be, and our modelling procedure accounts for them.

Kinematic classification and properties. The kinematic information was derived from the SINFONI and KMOS data cubes following well-established methods^{3,8,80} (all details of the data reduction and calibration procedures can also be found in these references). In summary, for each galaxy we fitted Gaussian line profiles to each spatial pixel of the IFS sample in the final reduced data cube, in some cases after some prior smoothing to increase signal-to-noise ratios. The main kinematic parameters of interest (v_{rot} , σ_0 and PA_{kin}) are then derived from the resulting spatially resolved maps of the velocity centroid and velocity dispersion. The quantity v_{rot} is the maximum rotation velocity, corrected for beam smearing and inclination i ($v_{\text{rot}} = c_{\text{psf},v} v_{\text{obs}} / \sin(i)$), where v_{obs} is half of the difference between the maximum positive and negative velocities on both sides of the galaxy, and $c_{\text{psf},v}$ is the beam-smearing correction for velocity. The quantity σ_0 is the intrinsic velocity dispersion, corrected for beam smearing ($\sigma_0 = c_{\text{psf},\sigma} \sigma_{\text{obs}}$), where σ_{obs} is the measured line width in the outer parts of the galaxy, corrected for instrumental spectral resolution (that is, subtracting in quadrature σ_{instr}), and $c_{\text{psf},\sigma}$ is the beam-smearing correction for the velocity dispersion. PA_{kin} is the position angle of the kinematic major axis passing through the extrema of the velocity field (the ‘line of nodes’). The beam-smearing corrections were derived on the basis of model disks for a range of masses, inclinations, ratios of galaxy to beam size, and radii of measurement appropriate for the SINS/zC-SINF and KMOS^{3D} datasets; all details are given in appendix A of ref. 35.

With these kinematic maps and properties, a galaxy is classified as a ‘rotation-dominated’ disk if⁸

- (1) the velocity map exhibits a continuous velocity gradient along a single axis (in larger systems with good signal-to-noise ratios, this is synonymous with the detection of a ‘spider’ diagram in the two-dimensional, first moment velocity map⁸¹);
- (2) $v_{\text{rot}}/\sigma_0 > 1$;
- (3) the position of the steepest velocity gradient, as defined by the midpoint between the velocity extrema along the kinematic axis, is coincident within the uncertainties with the peak of the velocity dispersion map;
- (4) the morphological and kinematic major axes are in agreement ($\leq 30^\circ$); and
- (5) the kinematic centre of the galaxy coincides with the maximum/centroid of the stellar distribution.

For the seeing-limited KMOS^{3D} survey, 83% of the resolved galaxies fulfil criteria (1) and (2) (92% at $z \approx 1$ and 74% at $z \approx 2$)⁸. This fraction slowly decreases as the stricter criteria (3), (4) and (5) are added, and amounts to 70% if all five

criteria are satisfied. Similar results are obtained in the other recent surveys^{61,64,78} (see also N.M.F.S. *et al.*, manuscript in preparation, for the SINS/zC-SINF sample).

The six individual galaxies discussed here, and the stacking sample, satisfy all of the above disk criteria on the basis of their SINFONI and KMOS data. With the higher signal-to-noise ratio of the deeper follow-up observations of the individual galaxies, additional asymmetric features became apparent in the kinematic maps of three of them, associated with gas inflows towards the centre (D3a 15504)⁷⁶ or gas outflows from the inner few kiloparsecs plausibly driven by an active galactic nucleus (AGN), and from bright off-centre clumps driven by star formation (D3a 15504, zC 406690, zC 400569 and D3a 6397)^{82–84}.

Kinematic analysis and mass modelling. Refs 14, 20 and 35 provide details of the kinematic analysis method used here, including details on the mathematical and fitting methodology, and refer to the publicly available data analysis tools in the ESO KMOS analysis pipeline, the LINEFIT tool⁸⁰, a generalized fitting tool (MPFIT) and the general cube analysis tool QFitsView (<http://www.mpe.mpg.de/~ott/QFitsView/>) that we used to fit the kinematics with a combination of an exponential disk and dark-matter haloes. In summary, in our kinematic analysis we proceed as follows.

(1) We fit a Gaussian profile to each spatial pixel of the data cube, suitably smoothed to deliver sufficiently high signal-to-noise ratio in the outer parts of the galaxy. We infer the systemic redshift (or velocity) of the galaxy by symmetrizing the redshifted and blueshifted peak velocities. We determine the position angle of the kinematic axis PA_{kin} by determining the line of nodes along the maximum velocity gradient, and that of the morphological major axis of the galaxy PA_{morph} from the stellar surface-density map or the H-band HST map, and take an average. These two angles typically agree to better than 5° – 7° . We determine the galaxy centre (x_0, y_0) from an average of the zero-crossing of the line of nodes, the velocity dispersion peak and the position of the central stellar bulge, which is prominent in all six of the galaxies studied. This enables us to determine (x_0, y_0) to about 0.5–1 pixels, which is small compared to the size of the final extraction slit in the next step. We infer the inclination of the disk from the minor-to-major axis ratio $q = b/a$ of the stellar distribution or the HST H-band data, and $\cos^2(i) = (q^2 - q_0^2)/(1 - q_0^2)$, with $q_0 \approx 0.15$ – 0.2 appropriate for $z \approx 1$ –3 (refs 14, 20, 35). We found in KMOS^{3D} that this method works reasonably well for inclined disks⁶, but becomes very uncertain for the three face-on disks in our sample, D3a 15504, zC 406690 and D3a 6397. In these cases we included the inclination as a second-order fit parameter to bring the disk mass into a good match with the prior $M_{\text{baryon}} = M_{\text{bulge}} + M_{\text{disk}} + M_{\text{gas,disk}}$, where $M_{\text{gas,disk}}$ is the mass of gas in the baryonic disk.

(2) Next we go back to the original data cube and extract position–velocity and position–velocity–dispersion cuts along the best-fit major axis by fitting Gaussian profiles in software slits typically 4–5 pixels perpendicular to, and 2–3 pixels along the line of nodes. This corresponds to about 1.1 and 0.5 resolution elements, respectively, and so is approximately Nyquist sampled along the line of nodes. To include systematic uncertainties, we multiply all fit errors by 1.5 and introduce lower ceiling uncertainties of $\pm 5 \text{ km s}^{-1}$ and $\pm 10 \text{ km s}^{-1}$ for velocity and velocity dispersion measurements, respectively. These scalings are derived from bootstrapping and from error scaling of the final reduced chi-squared χ_r^2 to about 1 for five of the six sources. We do not consider the additional information from deviations from Gaussian shape (the third and fourth moments, h_3 and h_4)⁸⁵; these deviations do not provide any additional useful information for the outer disks, only details of the heavily beam-smear data in the cores of the galaxies, which is of secondary interest here. We then subtract in squares the instrumental line width to infer the intrinsic velocity dispersions in each slit.

(3) Now we begin the fitting process to a model that consists of an $n = 1$ exponential disk (with effective radius $R_{1/2,\text{disk}}$), a central bulge of radius $R_{\text{bulge}} = 1$ kpc (with the B/T fit parameter giving the mass in the bulge relative to the total (disk + bulge) baryonic mass $M_{\text{baryon,disk}}$ and the remaining mass being in the $n = 1$ disk) and a dark-matter halo. In the cases in which we have a large bulge, we assume that the H α light distribution traces only the disk component, which is empirically justified^{60,62}. The assumption of exponential disk distributions ($n = 1$) is well supported for the 3D-HST star-forming population, which is characterized by $n = 0.5$ – 2 for all but the more bulge-dominated systems^{6,57}. We assume that the disk has a constant velocity dispersion, which we determine mainly in the outer parts of each galaxy where the beam-smear rotation component is small. For the fitting we use a thin exponential disk rotation curve²¹, but correct for the effects of the large scale height ($h_z \approx (\sigma_0/v_{\text{rot}}(R_{1/2}))R_{1/2}$) with models⁸⁶ that assume a constant scale height. Near $R_{1/2}$, the Freeman disk rotates 15% faster than the corresponding spherical model, and the Noordermeer correction is about 0.9–0.97 so that the final rotation velocity is only 4%–11% faster than the spherical model. For the dark-matter halo, we use an NFW²² model. We do not consider adiabatic contraction of the halo, so the only parameter of the halo is its mass $M_{\text{virial}} = M_{200(\text{NFW})}$, where $M_{200(\text{NFW})}$ is the mass within the radius at which the

mean density exceeds 200 times the critical density of the Universe, and where we fix the concentration parameter c to a typical value at the respective redshift^{87–89}. The angular momentum parameter of the halo is implicitly contained in $R_{1/2,\text{disk}}$ and the assumption that $j_{\text{disk}} = j_{\text{DM}}$, where j_{disk} and j_{DM} are the specific angular momenta of the baryonic disk and the dark matter, respectively³⁵. This yields five or six primary fit parameters: $R_{1/2,\text{disk}}$, $M_{\text{baryon,disk}}$, M_{virial} , B/T , σ_0 and, in three cases, the disk inclination i . As for the data we determine velocity and velocity dispersion cuts for the model, convolve with the instrumental beam and then find the weighted best fit in the usual chi-squared minimization (using the DYSMAL tool)^{6,80}. For four or five of these parameters we have priors from independent data: i , B/T and $R_{1/2}$ from the HST J, H imagery, $M_{\text{baryon,disk}}$ from the sum of the stellar disk mass in the bulge and in the disk from the 3D-HST modelling, and the (molecular) gas mass M_{molgas} from the scaling relations between M_* , star-formation rate, z and M_{molgas} (refs 25, 53). We use these priors and their uncertainties to set upper and lower limits for the fitting range, and a constraint for inclination, as described above. The mass of the dark-matter halo M_{virial} is a free parameter in the fitting, with only a fixed lower limit of $M_{\text{virial}} = 10^7 M_\odot$.

(4) We include in our fitting a correction of the disk rotation to account for pressure effects due to the large turbulent motions (asymmetric drift)^{6,14,35}. This correction lowers the rotation velocity in the outer disk:

$$v_{\text{rot}}^2 = v_c^2 + 2\sigma^2 \frac{d(\ln\Sigma)}{d(\ln R)} = v_c^2 - 2\sigma^2 \frac{R}{R_d} \quad (1)$$

where Σ is the surface-density distribution of the disk, which we assume to be an exponential with scale length $R_d = R_{1/2}/1.68$. The assumption of radially constant velocity dispersion, which implies that the thickness of the disk increases exponentially with radius, is probably a simplification. A superposition of a thin and thick disk could lead to a radially increasing dispersion and a more steeply falling rotation curve, which would enable a higher dark-matter fraction for $R \geq R_{1/2}$ than in the case of constant dispersion. In the absence of clear evidence, we retain the simplest assumption of a constant velocity dispersion.

Extended Data Fig. 2 shows the final χ^2_{r} distributions for the most important parameter for our study, the dark-matter fraction at $R_{1/2}$, $f_{\text{DM}}(R_{1/2})$. The number of independent data points in the six galaxies varies from 30 to 54, and with the error-scaling described above the best fit in five of the six galaxies has a minimum of $\chi^2_{\text{r,min}} = 0.98$ –1.7. The one exception, D3a 15504 (black line in Extended Data Fig. 2), has $\chi^2_{\text{r,min}} = 2.25$, owing mainly to the overshooting of the central velocity dispersion in two independent datasets that cannot be matched by the bulge + disk data, and to a second outlier point in velocity just north of the nucleus. We believe that the cause of these large near-nuclear deviations from the model is strong non-circular or bar streaming in combination with outflows from the central AGN, which are well known to exist in this galaxy^{76,84}. We return briefly to this issue when we discuss the two-dimensional residual maps below.

Parameter correlations and dark-matter fractions. From Extended Data Fig. 2 it becomes clear that the $\chi^2_{\text{r}}-f_{\text{DM}}(R_{1/2})$ space is relatively flat for some of the studied galaxies, and so it is important to systematically test the dependence of $f_{\text{DM}}(R_{1/2})$ on physical properties that constrain the rotation curve other than M_{baryon} and the mass of the dark-matter halo M_{DM} , namely $R_{1/2}$ and B/T . For galaxies with very low $f_{\text{DM}}(R_{1/2})$ (zC 400569 and zC 406690), varying $R_{1/2}$ within the uncertainties, or B/T in steps of 0.05 or 0.1, does not greatly alter $f_{\text{DM}}(R_{1/2})$. For the other galaxies, changing B/T has a larger effect than does changing $R_{1/2}$. We find most extreme changes for D3a 6397, with $(\partial f_{\text{DM}})/(\partial B/T) = 2.4$ when going from the best-fit $B/T = 0.35$ to $B/T = 0.3$ (that is, towards lower $f_{\text{DM}}(R_{1/2})$), and with $(\partial f_{\text{DM}})/(\partial R_{1/2}) = 0.6$ when going from the best-fit $R_{1/2} = 0.87$ to $R_{1/2} = 0.97$ (that is, towards higher $f_{\text{DM}}(R_{1/2})$). We show schematically in Extended Data Fig. 3 the ways in which f_{DM} and χ^2_{r} change for changes in these various parameters.

Generally, we find that increasing B/T leads to increased $f_{\text{DM}}(R_{1/2})$, which can be understood in the sense that a higher baryonic mass fraction in the central bulge decreases the relative contribution of the baryons to v_c at $R_{1/2}$. When changing $R_{1/2}$, the effects are less definite, but for the majority of cases we find that increasing $R_{1/2}$ again leads to increased $f_{\text{DM}}(R_{1/2})$. For these cases, this result can be understood in the sense that a larger $R_{1/2}$ distributes the baryonic mass onto a larger disk (that is, less compact), leading to less relative contribution of the baryons to v_c at $R_{1/2}$. Mean changes in $f_{\text{DM}}(R_{1/2})$ when increasing or decreasing the best-fit $R_{1/2}$ by the uncertainties given in Table 1, or when increasing or decreasing the best-fit B/T by 0.1, are all below $\Delta f_{\text{DM}} = 0.13$ (see also Extended Data Fig. 3).

The dark-matter fraction depends also on the mass distribution of the halo. Our best-fit models do not include the possible adiabatic contraction of the dark-matter halo as a response to the formation of the central galaxy. Simulations show that, at high redshift ($z \approx 2$), adiabatic contraction can have an effect on the central dark-matter density distribution^{90,91}. Its net effect, however, is not well constrained and depends largely on the feedback implementation⁹², where strong supernova

or AGN feedback can even create central dark-matter cores^{93,94}. Recent work⁹⁵ constructs a toy model of repeated inflow and outflow cycles for dwarf- to Milky-Way-type haloes to capture the various effects of baryons on the central dark-matter distribution. The results show that high gas fractions and low star-formation efficiencies favour halo expansion and extended baryon distributions. Another possibility is ‘baryonic gas-pile-up’ at early times⁹⁶. Because the star-formation accretion rate scales as $(1+z)^{2-3}$ (ref. 103), whereas the star-formation efficiency scales as $(1+z)^{0.6}$ (ref. 25), star formation may not be efficient enough at $z > 2-3$ to consume the incoming accreted baryonic gas, and so gas might pile-up in the inner disk⁹⁶.

We tested the effect of adiabatic contraction on an NFW halo⁹⁷. Generally, for the constraints on the dark-matter halo set by our data, we find that the effects of adiabatic contraction (or of modest variations of the concentration parameter) on f_{DM} are not as strong as the effects of changing $R_{1/2}$ or B/T within the uncertainties (Extended Data Fig. 4).

Two-dimensional analysis. Our analysis so far has used major-axis cuts of velocity and velocity dispersion to characterize the mass distribution. We used the two-dimensional information of integral field data to constrain (x_0, y_0) and PA_{kin} . The question is whether two-dimensional fitting of the gas kinematics might provide additional constraints. For the relatively low-resolution data for compact high-redshift disks (with $R_{1/2,\text{disk}}/R_{1/2,\text{beam}} \approx 2.7$ –4.5), most of the rotation-curve information is indeed encapsulated on or near the major axis. In deep AO data on moderate-inclination, large disks, a kinematic estimate of inclination can be obtained from the off-axis data, in addition to centre and node direction. The 22-h SINFONI AO data for D3a 15504 (N.M.F.S. *et al.*, manuscript in preparation) can be used in this way, and Extended Data Fig. 5 shows the result. In this case, the analysis of the data from the minor-axis cut supports the evidence from the HST stellar distribution and the baryonic-to-dynamical mass constraint that the inclination of this galaxy is low, $34^\circ \pm 5^\circ$ (Table 1).

Kinematic residual maps. Another way of using the full two-dimensional information is to construct two-dimensional residual maps (data minus model) of velocity and velocity dispersion, constructed from the major-axis-cut method, and then to check whether systematic residuals appear⁸¹. Extended Data Fig. 6 shows the residual maps for the six galaxies.

The residual maps show that the simple model of a compact bulge, $n = 1$ thick disk and NFW halo does a fairly good job at accounting for the data. With two or three exceptions discussed below, most of the residual maps do not show large-scale features or strong deviations that are comparable to the amplitudes in the original maps. Average values in the 12 residual maps range between -10 km s^{-1} and $+10 \text{ km s}^{-1}$, a few per cent of the maximum data range. The median dispersions of the residuals range from 8 km s^{-1} to 18 km s^{-1} , comparable to the measurement errors in most individual pixels, with two exceptions.

Kinematic anomalies. D3a 15504. One outlier is the galaxy D3a 15504 (top left in Extended Data Fig. 6). As discussed previously⁷⁶, the strong ($\pm 65 \text{ km s}^{-1}$) velocity gradient near the nucleus, but along the minor axis of the galaxy, had been apparent, which the deeper data confirm. Related to this minor-axis streaming, and probably also influenced by a strong, broad nuclear outflow component⁸⁴, is the high value of the nuclear velocity dispersion (about 175 km s^{-1}), which cannot be accounted for by the best-fitting disk model and so shows up as a large outlier in the velocity-dispersion residual map. D3a 15504 has a small neighbour about $1.5''$ northwest of the nucleus (position angle of -45° , visible in the stellar-density contour map in Fig. 1), which has a mass $(2-3) \times 10^9 M_\odot$ —about 3% of the stellar mass of the main galaxy. H α emission from the satellite is detected in our deep integral field data at a projected velocity of around $+10 \text{ km s}^{-1}$ (relative to the systemic velocity of the main galaxy)—about 140 km s^{-1} redshifted relative to the projected rotation velocity of the main galaxy at this radius. The neighbour therefore is a satellite. The position-velocity diagram of H α emission shows that the satellite is connected back to the main galaxy, clearly indicating that the two are interacting. We removed the well-separated H α emission of the satellite before fitting the rotation curve in Fig. 1.

zC 406690. zC 406690, shown in the middle row of the left-hand column in Extended Data Fig. 6, also exhibits a large anomaly in the residual maps of both velocity and velocity dispersion, in the outer southwestern part of the rotating ring structure, on and near ‘clump B’^{82,83}. This anomaly is caused by localized, blueshifted, very broad (up to $-1,000 \text{ km s}^{-1}$) H α emission near that clump, and can probably be explained by star-formation-driven outflows. zC 406690 also has a companion located about $1.6''$ west of the main ring galaxy, with a stellar mass of $6 \times 10^9 M_\odot$ (14% of the main system). There is a marginal detection of H α from that companion at around $+100 \text{ km s}^{-1}$ relative to the systemic velocity of the main galaxy, implying that it is an interacting satellite.

zC 400569. zC 400569, the bottom galaxy in the left-hand column in Extended Data Fig. 6, has two neighbours. Both are fairly prominent in H α , but are not detected in [N II], plausibly because of their low mass and metallicity. The larger

one, with a stellar mass of about $7 \times 10^9 M_\odot$ (5% of the mass of the main galaxy, $1.3 \times 10^{11} M_\odot$), is $1''$ southeast of the nucleus of zC 400569, with a projected velocity in H α of -330 km s^{-1} , and appears to be edge on, but does not exhibit much of a velocity gradient along its major axis. The second neighbour, $1.5''$ to the southeast, has a stellar mass of $3 \times 10^9 M_\odot$ (2.3% of the main galaxy) and shows an east–west velocity gradient of $\pm 20 \text{ km s}^{-1}$ around the centre, which is blueshifted by -410 km s^{-1} relative to the main galaxy. It therefore seems that zC 400569 is situated in a group of gas-rich, satellite galaxies of low mass and metallicity. The effect of the first galaxy on the line profiles is visible in the lower left of the residual maps of velocity and velocity dispersion Extended Data Fig. 6, but does not greatly affect the dynamical analysis in Fig. 1.

Neighbours and warps. Our analysis of the HST and H α data of the six galaxies shows that five sample galaxies have neighbours projected within $1''$ and $3.3''$ (8–25 kpc) of the main galaxy, and between 1% (GS4 43501, $4 \times 10^8 M_\odot$) and 20% (COS4 01351, $1.2 \times 10^{10} M_\odot$) of its mass. Of those five, the detection of H α emission from the companion in three (D3a 15504, zC 400690 and zC 400569) shows that these companions are indeed interacting satellites, but probably not in the other two galaxies (COS4 01351 and GS4 43501).

The Jacobi (or Roche or Hills) radius in a double galaxy system with masses M_1 and M_2 , separated by R_{12} , defines the distance from the lower-mass system M_2 within which tidal forces by the smaller system strongly perturb particles in the bigger system. This radius is given by (ref. 98, Ch. 8)

$$r_J = \left(\frac{M_2}{3M_1} \right)^{1/3} R_{12} = 3 \text{ kpc} \left(\frac{M_2/M_1}{0.05} \right)^{1/3} \frac{R_{12}}{12 \text{ kpc}}$$

Here we have inserted the typical mass ratios and separations for the satellite–main-galaxy systems in our sample. This simple analysis shows that tidal perturbations or stripping by the satellite can be important in the outer parts of the main galaxies, if the satellite is within about $R_{1/2}$ of the main galaxy, as seems to be the case for, for instance, the northwestern satellite of D3a 15504.

In addition to interactions, warping can be important in the outer disks and is frequently observed in the outer H I layers of $z \approx 0$ galaxies (including the Milky Way)⁹⁹. Theoretically, this type of buckling or firehose instability (with a predominant $m = 2$ mode) can occur in galaxy disks with surface density Σ , with radial wavelengths of $\lambda \leq \lambda_J = \sigma_x^2 / (G\Sigma)$, where σ_x is the in-plane velocity dispersion (ref. 98, Ch. 6.6.1; ref. 100) and G is the gravitational constant, if the system is sufficiently cold in the vertical direction for the instability to grow, which requires^{100,101} $h_z < \sigma_z^2 / (G\Sigma)$ such that $\sigma_z / \sigma_x < 0.3\text{--}0.6$, where σ_x is the velocity dispersion in the galaxy plane and h_z is the disk scale-height. The current data for high-redshift galaxies suggest that the velocity dispersion ellipsoid is isotropic^{4,82} ($\sigma_x = \sigma_z$), such that warping should be suppressed.

If the warp has sufficiently high amplitude, then it could introduce a radial dependence of the peak rotation velocity along the major axis. If the dominant mode is odd ($m = 1$, or $m = 3$ as in the Milky Way)¹⁰², then warps would also introduce the same sign of the change in the absolute value of the peak rotation curve on the blueshifted and redshifted side of the galaxy, which could mimic a radial decrease (or increase) in the rotation curve, with equal probability. However, no substantial increase is seen in any of the galaxies of the SINS/zC-SINF or KMOS^{3D} samples. If the mode is even ($m = 2$), then we expect to observe rotation curves that increase on one side and decrease on the other, but we do not observe this feature in any of the six galaxies presented. Finally, the phase of the warp does not have to be aligned with the major axis and might change with radius. Such precessions could be observed in the residual maps; however, the data do not show any evidence for such an effect.

Comments on overall strategy. Here we put forward observational evidence for very high baryon fractions (and correspondingly low dark-matter fractions) in several high-mass disk galaxies at $z \approx 1\text{--}2$. First hints at this result came from H α kinematics studies initially in the SINS sample³ and more robustly in the KMOS^{3D} sample^{6,8} and, independently by others, in compact high-redshift star-forming galaxies⁴ and in the MOSDEF survey⁵. In most cases, the dynamical masses of the inner star-forming disks of $z \approx 1\text{--}2.5$ star-forming galaxies are inferred from the peak H α rotation velocity (or velocity dispersion), and then are compared with the baryonic mass, that is, the sum of the stellar mass and the cold-gas mass. The stellar mass is estimated from population synthesis fitting of the ultraviolet/optical SEDs, and the gas mass from CO or dust tracing the molecular hydrogen content^{3–6,25}. Unfortunately, this first ‘inner-disk dynamics’ technique, even in the best cases of spatially well-resolved kinematics, requires strong assumptions on star-formation histories, initial stellar-mass functions and calibrations of CO/dust emission to H₂ mass that are inherently not known to better than ± 0.2 dex to ± 0.25 dex. Nearly 50 years of experience of local Universe studies have taught us that robust statements on dark-matter content cannot be made solely, and certainly not robustly, on the basis of the ‘inner-disk dynamics’ technique¹⁰³.

More robust statements on dark-matter fractions are expected to come from rotation curves in the outer disk and inner halo. In a second approach, we detected a few cases of potentially falling H α rotation curves in the best SINS/zC-SINF data a few years ago, but it took several years to collect enough integration time to make a solid case for the six galaxies reported here. However, these cases are biased because we invested additional integration time only in galaxies for which we already had evidence of falling rotation curves. To check that these galaxies are not outliers in a population of star-forming galaxies with primarily flat rotation curves, we needed a statistical statement on the occurrence of falling rotation curves in the high-redshift, massive star-forming population, even if the individual rotation curves in these other galaxies were individually not good enough for study. As the KMOS^{3D} sample grew in size, we therefore developed as a third element of our strategy—a ‘rotation curve stacking’ technique on the overall sample to test for the hypothesis that the individual cases were (or were not) outliers. The results of this project¹⁸ confirm that falling rotation curves appear to be common at $z \approx 1\text{--}2.5$; see Methods section ‘Stacking analysis’ for a summary and ref. 18 for the exhaustive technical discussion of the methodology required to demonstrate the robustness of the result.

A fourth approach in this overall strategy is the measurement of the zero-point offsets of the baryonic and stellar mass Tully–Fisher relation as a function of redshift. This ‘Tully–Fisher zero-point evolution’ approach is related to the ‘inner-disk dynamics’ method above, but uses the redshift dependence of a population-averaged property (the Tully–Fisher zero-point) instead of relying on the accurate determination of baryon fractions in individual galaxies. The results of the Tully–Fisher technique for the KMOS^{3D} sample (H.Ü. *et al.*, manuscript in preparation) are in agreement with the other three tests.

Stacking analysis. In the following we summarize the stacking analysis of ref. 18.

Having established the properties of a few high-quality outer-disk rotation curves in star-forming galaxies with long integrations, the next step is to characterize the average rotation curve of a representative sample of $z \approx 0.6\text{--}2.6$ massive star-forming disks, as drawn from the seeing-limited KMOS^{3D} and AO-assisted SINS/zC-SINF datasets. For this purpose, a stacking approach was used to systematically determine the shape of the outer rotation curves.

This stacking method is designed to leverage the faint outer ionized gas emission combining the signal of more than 100 massive star-forming galaxies at $0.6 < z < 2.6$. The methodology first includes the normalization of each individual rotation curve by its observed maximum velocity v_{max} and the corresponding turnover radius R_{max} . Both v_{max} and R_{max} are determined by fitting the rotation curve with an exponential disk model convolved with the appropriate instrumental resolution of the dataset. Values for R_{max} are also independently derived for each galaxy by converting intrinsic half-light radii measured on rest-frame optical HST images into observed turnover radii, taking into account the effect of beam smearing and the shape of the mass distribution (as parameterized by the Sérsic index). These independently derived R_{max} values are in good agreement with the R_{max} values measured on the actual rotation curves and thus substantiate the validity of our R_{max} measurements using pure exponential disk models. On the basis of mock galaxy simulations, the above technique of normalizing and stacking rotation curves is demonstrated¹⁸ to be able to reproduce both outer falling and rising rotation curves, with the latter being expected if massive star-forming galaxies at high redshift are genuinely more dark-matter-dominated.

With R_{max} and v_{max} derived for each galaxy, normalized position–velocity diagrams are generated, which are then averaged into a stack from which a final combined rotation curve is constructed. Owing to field-of-view limitations for both KMOS and SINFONI AO observations, the number of galaxies available at a given galacto-centric radius drops with distance to the centre, such that the combined stacked rotation curve can be reliably determined out to about $2.4R_{\text{max}}$, which corresponds to several effective radii. Within this radius, the shape of the resulting stack outlines a fall-off in rotation velocity beyond R_{max} , symmetrically on either side from the centre, reaching down to about $0.65v_{\text{max}}$. We show in Fig. 2a a slightly altered version of the original stack, where we have removed D3a 15504, zC 400569 and GS4 43501 so that the remaining stack and the individual rotation curves are completely independent of each other. The study utilizes template rotation curves of local spiral galaxies¹⁹ and shows that the outer fall-off in the stacked rotation curve deviates substantially from the (mildly rising) average rotation curves of local analogues of similar mass at the same galacto-centric radii.

In addition, the study¹⁸ evaluates the outer drop in the stack by comparing with models that include baryons arranged in an exponential disk configuration with added dark-matter NFW haloes, taking into account pressure gradients in the outer disk resulting from large velocity dispersion. This comparison demonstrates that the stacked rotation curves can be explained by high baryonic disk mass fractions ($m_d = M_{\text{baryon}}/M_{\text{DM}} \geq 0.05$), in combination with large pressure support in the outer disk. The latter is accounted for by considering a value $4.8 < v_{\text{rot}}/\sigma_0 < 6.3$.

depending on radius, as found to be the average for the sample of stacked galaxies. Considering galaxies with strong pressure support (represented by low v_{rot}/σ_0) for stacking, the resulting averaged outer rotation curve steepens compared to a stack made with only high- v_{rot}/σ_0 galaxies, which supports the conclusion that a substantial part of the outer fall-off in the stacked rotation curve is driven by the presence of pressure effects in the outer disk.

The stacking study furthermore demonstrates that the above results are largely independent of the underlying model assumptions, such as the presence or absence of a central stellar bulge, the halo concentration parameter c and the possible adiabatic contraction of the host halo, because these do not seem to greatly alter the shape of the expected rotation curve.

The above results are in good agreement with the conclusion drawn from the six individual rotation curves presented here. Most importantly, the stacking confirms that outer falling rotation curves are a common feature among a larger representative sample of massive star-forming galaxies at high redshift.

Comparison to simulations. In the following, we discuss how our results compare to state-of-the-art cosmological simulations of galaxy formation, and briefly comment on the ‘thick disk’ phenomenon in local spiral galaxies.

Any quantitative comparison between observations and simulations is hindered by the fact that fundamental properties of high-redshift galaxies are not matched by the large-volume simulations that are needed to produce the observed diverse galaxy populations, and by disk galaxies that are already massive at $z \approx 2$. In addition, the effective co-moving spatial resolutions in current simulations, such as Illustris and Eagle, are 1–3 kpc, which are not, or are only barely, sufficient to resolve bulges, giant star-forming clumps and other intra-galactic structures, and the observed high star-formation rates and gas fractions are under-predicted in these simulations^{104,105}. Having said that, peaked rotation curves are produced in current simulations mostly as a result of weak (or no) feedback^{106,107}. However, it is now a consensus that stronger feedback descriptions (momentum feedback from supernovae or from AGN) are needed to match many other observed galaxy properties, such as outflows, disk-like morphology and angular momentum^{108–117}.

Given the limitations outlined above, a one-to-one comparison of our results with simulations is not feasible. However, to qualitatively compare simulations with our $z \approx 2$ galaxies, we use results from the Illustris cosmological hydro-simulation. To do so, we select galaxies at $z = 2$ with stellar masses satisfying $10.9 < \log(M_*/M_\odot) < 11.3$ and star-formation rates of more than $55 M_\odot \text{ yr}^{-1}$ —a total of 80 galaxies. Their mean properties in terms of stellar size, star-formation rate and stellar mass are $\langle R_{1/2,*} \rangle = 5.6$ kpc, and $\langle \text{SFR} \rangle = 120 M_\odot \text{ yr}^{-1}$, $\langle M_* \rangle = 1.2 \times 10^{11} M_\odot$, respectively. We then inspect the two-dimensional distributions of velocity and velocity dispersion, for which a cut of star-formation-rate surface density, $\Sigma_{\text{SFR}} > 0.01 M_\odot \text{ yr}^{-1} \text{ kpc}^{-2}$, has been applied. Galaxies are classified as rotationally supported if they exhibit a continuous velocity gradient along a single axis and if the velocity dispersion map displays a central peak that coincides with the kinematic centre of the galaxy. These criteria are fulfilled for about 50% of the galaxies. Judging from the velocity and velocity dispersion maps, about 25% of the rotationally supported Illustris galaxies exhibit falling rotation curves, that is, 10%–15% of the parent sample of 80 $z = 2$ star-forming galaxies.

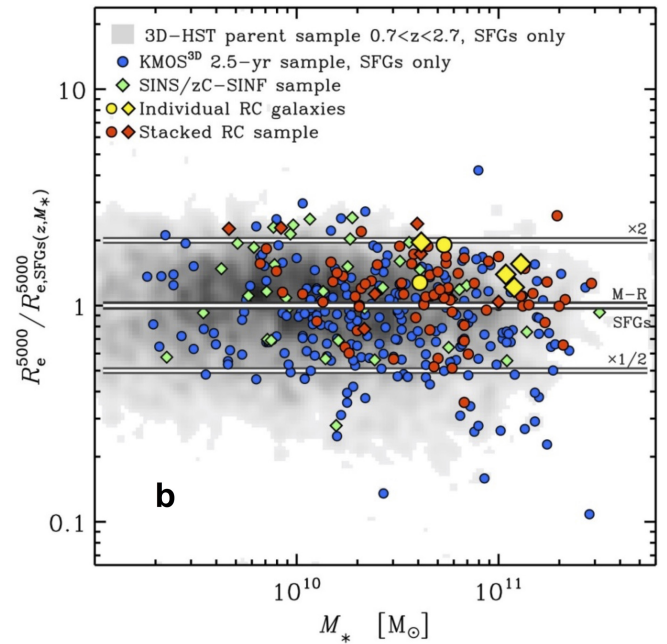
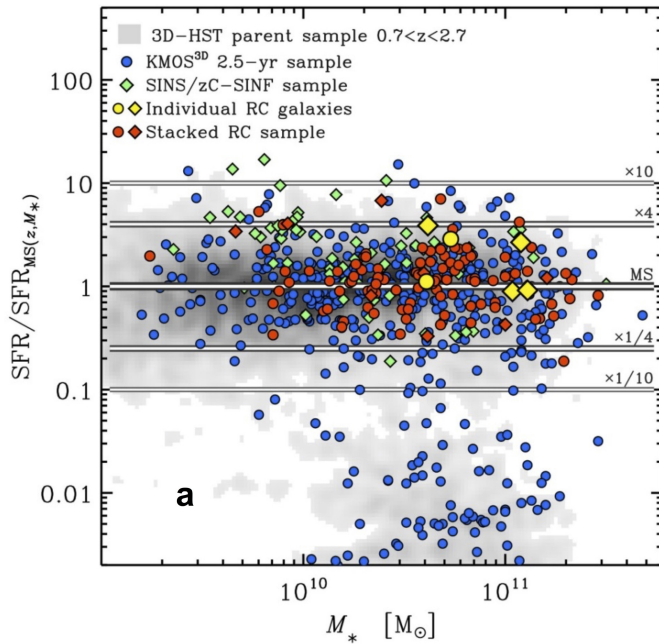
In other simulations, falling rotation curves are typically seen for very compact systems, which do not represent the main population of simulated (or observed) star-forming galaxies. Most simulations find larger v_{rot}/σ_0 than seen in the observed system, perhaps owing to their modest spatial resolutions not capturing all of the necessary intra-galactic physics mentioned above. Typical intrinsic velocity dispersions of the Illustris sample are 30–40 km s^{−1}. Peaked rotation curves in zoom simulations at $z = 3$ have recently been connected to higher bulge-to-total fractions¹¹⁸. A large fraction of our high-redshift star-forming galaxies indeed have massive bulges. However, it has been found¹⁸ that the effect of a bulge on the shape of the outer rotation curve is negligible for our otherwise fairly extended star-forming galaxies. Although our observed galaxies are all star-forming and extended, these theoretical results provide support to our interpretation of the evolution of the studied galaxies with cosmic time: the massive, high-redshift star-forming galaxies will probably soon be quenched, and will then evolve on the passive sequence into local, massive early-type galaxies^{24,119}.

There is an intriguing similarity between the turbulent high-redshift disks and the ‘thick disk’ phenomenon in local spiral galaxies²⁰. The stellar population of the thick disk indicates a formation time of $z > 1-2$, whereas thin-disk formation started at $z \approx 1$ and continues until today. Therefore, it is conceivable that the high-redshift sample of disk galaxies shows the transition period from thick-disk to thin-disk formation.

Data availability. The data discussed here are available on the archive of the European Southern Observatory (http://archive.eso.org/eso/eso_archive_main.html).

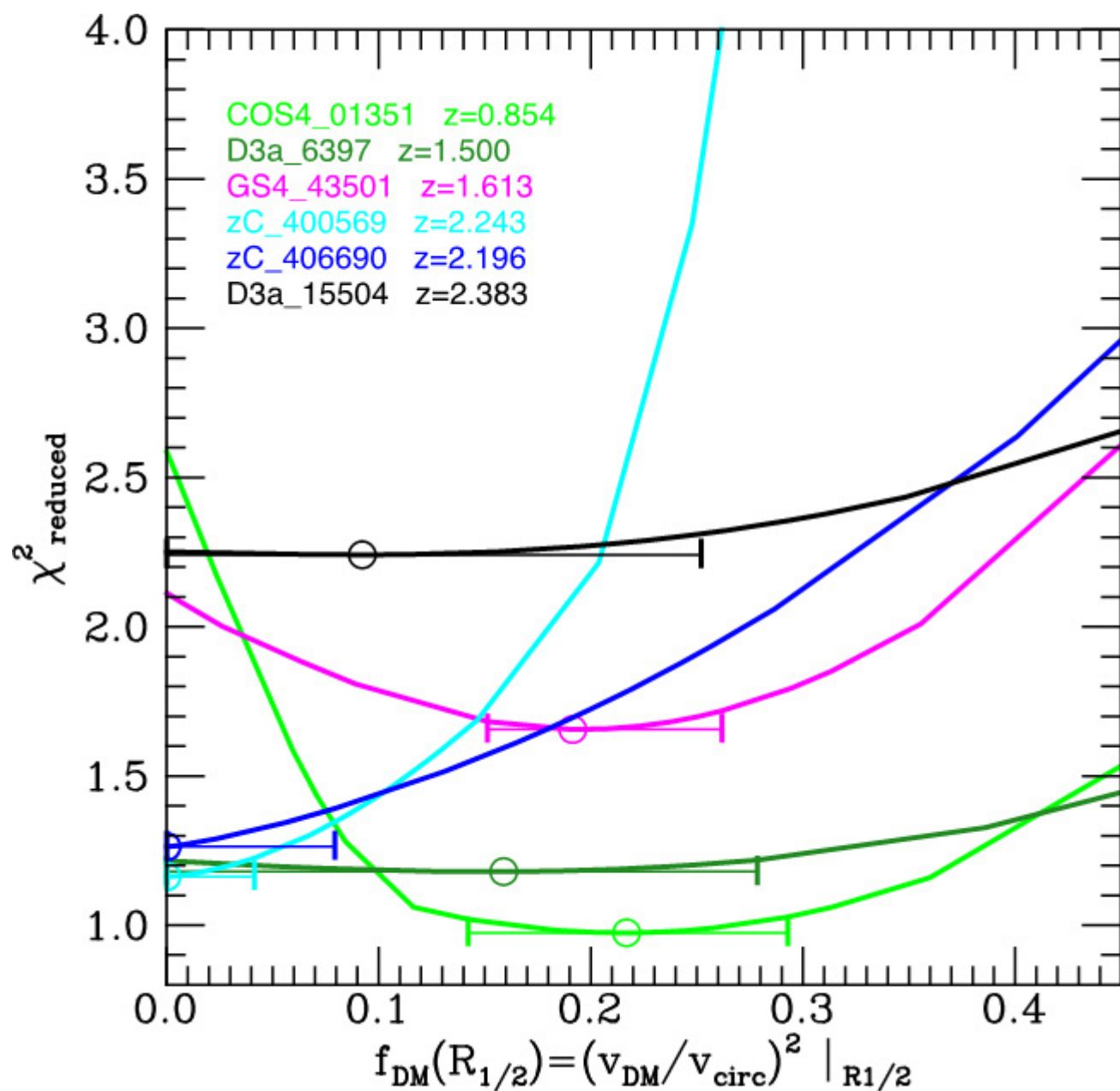
31. Mancini, C. *et al.* The zCOSMOS-SINFONI Project. I. Sample selection and natural-seeing observations. *Astrophys. J.* **743**, 86 (2011).
32. Eisenhauer, F. *et al.* The Universe in 3D: first observations with SPIFFI, the infrared integral field spectrometer for the VLT. *The Messenger* **113**, 17–25 (2003).
33. Bonnet, H. *et al.* First light of SINFONI at the VLT. *The Messenger* **117**, 17–24 (2004).
34. Sharples, R. M. *et al.* First light for the KMOS multi-object integral field spectrometer. *The Messenger* **151**, 21–23 (2012).
35. Burkert, A. *et al.* The angular momentum distribution and baryon content of star-forming galaxies at $z \sim 1-3$. *Astrophys. J.* **826**, 214 (2016).
36. Skelton, R. E. *et al.* 3D-HST WFC4-selected photometric catalogs in the five CANDELS/3D-HST fields: photometry, photometric redshifts, and stellar masses. *Astrophys. J. Suppl. Ser.* **214**, 24 (2014).
37. Whitaker, K. E. *et al.* Constraining the low-mass slope of the star formation sequence at $0.5 < z < 2.5$. *Astrophys. J.* **795**, 104 (2014).
38. van Dokkum, P. G. *et al.* First results from the 3D-HST survey: the striking diversity of massive galaxies at $z > 1$. *Astrophys. J.* **743**, L15 (2011).
39. Wuyts, S. *et al.* On star formation rates and star formation histories of galaxies out to $z \sim 3$. *Astrophys. J.* **738**, 106 (2011).
40. Bruzual, G. & Charlot, S. Stellar population synthesis at the resolution of 2003. *Mon. Not. R. Astron. Soc.* **344**, 1000–1028 (2003).
41. Calzetti, D. *et al.* The dust content and opacity of actively star-forming galaxies. *Astrophys. J.* **533**, 682–695 (2000).
42. Chabrier, G. Galactic stellar and substellar initial mass function. *Publ. Astron. Soc. Pac.* **115**, 763–795 (2003).
43. Wuyts, S. *et al.* A consistent study of metallicity evolution at $0.8 < z < 2.6$. *Astrophys. J.* **789**, L40 (2014).
44. Wuyts, S. *et al.* The evolution of metallicity and metallicity gradients from $z = 2.7$ to 0.6 with KMOS^{3D}. *Astrophys. J.* **827**, 74 (2016).
45. Erb, D. K. *et al.* The mass-metallicity relation at $z \geq 2$. *Astrophys. J.* **644**, 813–828 (2006).
46. Zahid, H. J., Kewley, L. J. & Bresoline, F. The mass-metallicity and luminosity-metallicity relations from DEEP2 at $z \sim 0.8$. *Astrophys. J.* **730**, 137 (2011).
47. Zahid, H. J. *et al.* The FMOS-COSMOS survey of star-forming galaxies at $z \sim 1.6$. II. The mass-metallicity relation and the dependence on star formation rate and dust extinction. *Astrophys. J.* **792**, 75 (2014).
48. Stott, J. P. *et al.* A fundamental metallicity relation for galaxies at $z = 0.84-1.47$ from HiZELS. *Mon. Not. R. Astron. Soc.* **436**, 1130–1141 (2013).
49. Steidel, C. C. *et al.* Strong nebular line ratios in the spectra of $z \sim 2-3$ star-forming galaxies: first results from KBSS-MOSFIRE. *Astrophys. J.* **795**, 165 (2014).
50. Sanders, R. L. *et al.* The MOSDEF survey: mass, metallicity, and star-formation rate at $z \sim 2.3$. *Astrophys. J.* **799**, 138 (2015).
51. Wuyts, S. *et al.* What do we learn from IRAC observations of galaxies at $2 < z < 3.5$? *Astrophys. J.* **655**, 51–65 (2007).
52. Kewley, L. J. *et al.* Theoretical evolution of optical strong lines across cosmic time. *Astrophys. J.* **774**, 100 (2013).
53. Tacconi, L. J. *et al.* PHIBSS: unified scaling relations of depletion time and molecular gas fractions with cosmic time, specific star formation rate and stellar mass. Preprint at <https://arxiv.org/abs/1702.01140> (2017).
54. Förster Schreiber, N. M. *et al.* Constraints on the assembly and dynamics of galaxies. I. Detailed rest-frame optical morphologies on kiloparsec scale of $z \sim 2$ star-forming galaxies. *Astrophys. J.* **731**, 65 (2011).
55. Förster Schreiber, N. M. *et al.* Constraints on the assembly and dynamics of galaxies. II. Properties of kiloparsec-scale clumps in rest-frame optical emission of $z \sim 2$ star-forming galaxies. *Astrophys. J.* **739**, 45 (2011).
56. Wuyts, S. *et al.* Smooth(er) stellar mass maps in CANDELS: constraints on the longevity of clumps in high-redshift star-forming galaxies. *Astrophys. J.* **753**, 114 (2012).
57. Lang, P. *et al.* Bulge growth and quenching since $z = 2.5$ in CANDELS/3D-HST. *Astrophys. J.* **788**, 11 (2014).
58. Tacchella, S. *et al.* The confinement of star-forming galaxies into a main sequence through episodes of gas compaction, depletion and replenishment. *Mon. Not. R. Astron. Soc.* **457**, 2790–2813 (2016).
59. Tacchella, S. *et al.* Evolution of density profiles in high- z galaxies: compaction and quenching inside-out. *Mon. Not. R. Astron. Soc.* **458**, 242–263 (2016).
60. Wuyts, S. *et al.* A CANDELS-3D-HST synergy: resolved star formation patterns at $0.7 < z < 1.5$. *Astrophys. J.* **779**, 135 (2013).
61. Genzel, R. *et al.* The SINS/zC-SINF survey of $z \sim 2$ galaxy kinematics: evidence for gravitational quenching. *Astrophys. J.* **785**, 75 (2014).
62. Nelson, E. J. *et al.* Where stars form: inside-out growth and coherent star formation from HST H α maps of 3200 galaxies across the main sequence at $0.7 < z < 1.5$. *Astrophys. J.* **828**, 27 (2016).
63. Tacchella, S. *et al.* Evidence for mature bulges and an inside-out quenching phase 3 billion years after the Big Bang. *Science* **348**, 314–317 (2015).
64. Tacchella, S. *et al.* SINS/zC-SINF survey of $z \sim 2$ galaxy kinematics: rest-frame morphology, structure, and colors from near-infrared Hubble Space Telescope imaging. *Astrophys. J.* **802**, 101 (2015).
65. Wuyts, S. *et al.* Galaxy structure and mode of star formation in the SFR-mass plane from $z \sim 2.5$ to $z \sim 0.1$. *Astrophys. J.* **742**, 96 (2011).
66. Bell, E. F. *et al.* What turns galaxies off? The different morphologies of star-forming and quiescent galaxies since $z \sim 2$ from CANDELS. *Astrophys. J.* **753**, 167 (2012).
67. Bruce, V. A. *et al.* The bulge-disc decomposed evolution of massive galaxies at $1 < z < 3$ in CANDELS. *Mon. Not. R. Astron. Soc.* **444**, 1001–1033 (2014).

68. Bruce, V. A. *et al.* The decomposed bulge and disc size–mass relations of massive galaxies at $1 < z < 3$ in CANDELS. *Mon. Not. R. Astron. Soc.* **444**, 1660–1673 (2014).
69. Nelson, E. J. *et al.* Spatially resolved dust maps from Balmer decrements in galaxies at $z \sim 1.4$. *Astrophys. J.* **817**, L9 (2016).
70. Tadaki, K. *et al.* SXDF-ALMA 1.5 arcmin² deep survey: a compact dusty star-forming galaxy at $z = 2.5$. *Astrophys. J.* **811**, L3 (2015).
71. Tadaki, K.-i. *et al.* Bulge-forming galaxies with an extended rotating disk at $z \sim 2$. *Astrophys. J.* **834**, 135 (2017).
72. Barro, G. *et al.* Sub-kiloparsec ALMA imaging of compact star-forming galaxies at $z \sim 2.5$: revealing the formation of dense galactic cores in the progenitors of compact quiescent galaxies. *Astrophys. J.* **827**, L32 (2016).
73. van der Wel, A. *et al.* Geometry of star-forming galaxies from SDSS, 3D-HST, and CANDELS. *Astrophys. J.* **792**, L6 (2014).
74. Elmegreen, D. M. *et al.* Galaxy morphologies in the Hubble ultra deep field: dominance of linear structures at the detection limit. *Astrophys. J.* **631**, 85–100 (2005).
75. Law, D. R. *et al.* An HST/WFC3-IR morphological survey of galaxies at $z = 1.5$ – 3.6 . I. Survey description and morphological properties of star-forming galaxies. *Astrophys. J.* **745**, 85 (2012).
76. Genzel, R. *et al.* The rapid formation of a large rotating disk galaxy three billion years after the Big Bang. *Nature* **442**, 786–789 (2006).
77. Kassin, S. *et al.* The epoch of disk settling: $z \sim 1$ to now. *Astrophys. J.* **758**, 106 (2012).
78. Newman, S. F. *et al.* The SINS/zC-SINF survey of $z \sim 2$ galaxy kinematics: the nature of dispersion-dominated galaxies. *Astrophys. J.* **767**, 104 (2013).
79. Tacconi, L. J. *et al.* Phibss: molecular gas content and scaling relations in $z \sim 1$ – 3 massive, main-sequence star-forming galaxies. *Astrophys. J.* **768**, 74 (2013).
80. Davies, R. *et al.* How well can we measure the intrinsic velocity dispersion of distant disk galaxies? *Astrophys. J.* **741**, 69 (2011).
81. van der Kruit, P. C. & Allen, R. J. The kinematics of spiral and irregular galaxies. *Annu. Rev. Astron. Astrophys.* **16**, 103–139 (1978).
82. Genzel, R. *et al.* The Sins survey of $z \sim 2$ galaxy kinematics: properties of the giant star-forming clumps. *Astrophys. J.* **733**, 101 (2011).
83. Newman, S. F. *et al.* Shocked superwinds from the $z \sim 2$ clumpy star-forming galaxy, ZC406690. *Astrophys. J.* **752**, 111 (2012).
84. Förster Schreiber, N. M. *et al.* The SINS/zC-SINF survey of $z \sim 2$ galaxy kinematics: evidence for powerful active galactic nucleus-driven nuclear outflows in massive star-forming galaxies. *Astrophys. J.* **787**, 38 (2014).
85. Cappellari, M. Structure and kinematics of early-type galaxies from integral field spectroscopy. *Annu. Rev. Astron. Astrophys.* **54**, 597–665 (2016).
86. Noordermeer, E. The rotation curves of flattened Sérsic bulges. *Mon. Not. R. Astron. Soc.* **385**, 1359–1364 (2008).
87. Bullock, J. S. *et al.* Profiles of dark haloes: evolution, scatter and environment. *Mon. Not. R. Astron. Soc.* **321**, 559–575 (2001).
88. Gao, L. *et al.* The redshift dependence of the structure of massive Λ cold dark matter haloes. *Mon. Not. R. Astron. Soc.* **387**, 536–544 (2008).
89. Dutton, A. A. & Macciò, A. V. Cold dark matter haloes in the Planck era: evolution of structural parameters for Einasto and NFW profiles. *Mon. Not. R. Astron. Soc.* **441**, 3359–3374 (2014).
90. Johansson, P. H., Naab, T. & Ostriker, J. P. Gravitational heating helps make massive galaxies red and dead. *Astrophys. J.* **697**, L38–L43 (2009).
91. Dutton, A. A. *et al.* The response of dark matter haloes to elliptical galaxy formation: a new test for quenching scenarios. *Mon. Not. R. Astron. Soc.* **453**, 2447–2464 (2015).
92. Duffy, A. R. *et al.* Impact of baryon physics on dark matter structures: a detailed simulation study of halo density profiles. *Mon. Not. R. Astron. Soc.* **405**, 2161–2178 (2010).
93. Pontzen, A. & Governato, F. How supernova feedback turns dark matter cusps into cores. *Mon. Not. R. Astron. Soc.* **421**, 3464–3471 (2012).
94. Martizzi, D., Teyssier, R. & Moore, B. Cusp–core transformations induced by AGN feedback in the progenitors of cluster galaxies. *Mon. Not. R. Astron. Soc.* **432**, 1947–1954 (2013).
95. Dutton, A. A. *et al.* NIHAO IX: the role of gas inflows and outflows in driving the contraction and expansion of cold dark matter haloes. *Mon. Not. R. Astron. Soc.* **461**, 2658–2675 (2016).
96. Lilly, S. J. *et al.* Gas regulation of galaxies: the evolution of the cosmic specific star formation rate, the metallicity–mass–star-formation rate relation, and the stellar content of halos. *Astrophys. J.* **772**, 119 (2013).
97. Blumenthal, G. R. *et al.* Contraction of dark matter galactic halos due to baryonic infall. *Astrophys. J.* **301**, 27–34 (1986).
98. Binney, J. & Tremaine, S. *Galactic Dynamics* 2nd edn (Princeton Univ. Press, 2008).
99. van der Kruit, P. C. & Freeman, K. C. Galaxy disks. *Annu. Rev. Astron. Astrophys.* **49**, 301–371 (2011).
100. Toomre, A. On the gravitational stability of a disk of stars. *Astrophys. J.* **139**, 1217–1238 (1964).
101. Merritt, D. & Sellwood, J. A. Bending instabilities in stellar systems. *Astrophys. J.* **425**, 551–567 (1994).
102. Levine, E. S., Blitz, L. & Heiles, C. The vertical structure of the outer Milky Way H I disk. *Astrophys. J.* **643**, 881–896 (2006).
103. Courteau, S. *et al.* Galaxy masses. *Rev. Mod. Phys.* **86**, 47–119 (2014).
104. Genel, S. *et al.* Introducing the Illustris project: the evolution of galaxy populations across cosmic time. *Mon. Not. R. Astron. Soc.* **445**, 175–200 (2014).
105. Schaye, J. *et al.* The EAGLE project: simulating the evolution and assembly of galaxies and their environments. *Mon. Not. R. Astron. Soc.* **446**, 521–554 (2015).
106. Johansson, P. H., Naab, T. & Ostriker, J. P. Forming early-type galaxies in Λ CDM simulations. I. Assembly histories. *Astrophys. J.* **754**, 115 (2012).
107. Anglés-Alcázar, D. *et al.* Cosmological zoom simulations of $z = 2$ galaxies: the impact of galactic outflows. *Astrophys. J.* **782**, 84 (2014).
108. Governato, F. *et al.* Forming disc galaxies in Λ CDM simulations. *Mon. Not. R. Astron. Soc.* **374**, 1479–1494 (2007).
109. Scannapieco, C. *et al.* The formation and survival of discs in a Λ CDM universe. *Mon. Not. R. Astron. Soc.* **396**, 696–708 (2009).
110. Scannapieco, C. *et al.* The Aquila comparison project: the effects of feedback and numerical methods on simulations of galaxy formation. *Mon. Not. R. Astron. Soc.* **423**, 1726–1749 (2012).
111. Brook, C. B. *et al.* Hierarchical formation of bulgeless galaxies – II. Redistribution of angular momentum via galactic fountains. *Mon. Not. R. Astron. Soc.* **419**, 771–779 (2012).
112. Agertz, O., Teyssier, R. & Moore, B. The formation of disc galaxies in a Λ CDM universe. *Mon. Not. R. Astron. Soc.* **410**, 1391–1408 (2011).
113. Aumer, M., White, S. D. M. & Naab, T. Towards a more realistic population of bright spiral galaxies in cosmological simulations. *Mon. Not. R. Astron. Soc.* **434**, 3142–3164 (2013).
114. Hopkins, P. F. *et al.* Galaxies on FIRE (Feedback In Realistic Environments): stellar feedback explains cosmologically inefficient star formation. *Mon. Not. R. Astron. Soc.* **445**, 581–603 (2014).
115. Marinacci, F., Pakmor, R. & Springel, V. The formation of disc galaxies in high-resolution moving-mesh cosmological simulations. *Mon. Not. R. Astron. Soc.* **437**, 1750–1775 (2014).
116. Übler, H. *et al.* Why stellar feedback promotes disc formation in simulated galaxies. *Mon. Not. R. Astron. Soc.* **443**, 2092–2111 (2014).
117. Genel, S. *et al.* Galactic angular momentum in the Illustris simulations: feedback and the Hubble sequence. *Astrophys. J.* **804**, L40 (2015).
118. Fiacconi, D., Feldmann, R. & Mayer, L. The Argo simulation – II. The early build-up of the Hubble sequence. *Mon. Not. R. Astron. Soc.* **446**, 1957–1972 (2015).
119. Carollo, M. C. *et al.* Newly quenched galaxies as the cause for the apparent evolution in average size of the population. *Astrophys. J.* **773**, 112 (2013).



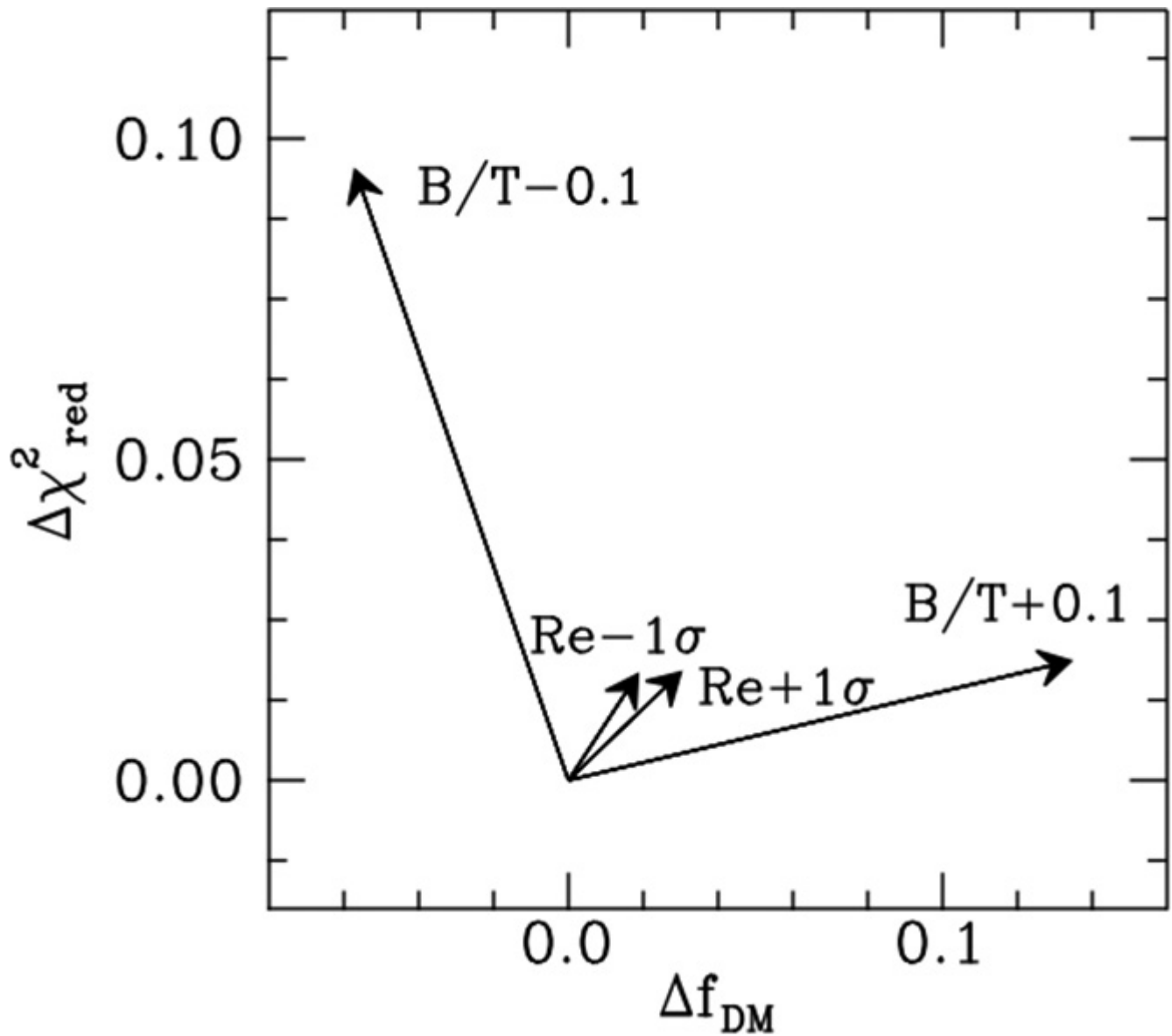
Extended Data Figure 1 | Location of the galaxies included in our analysis. **a**, Location in stellar-mass–star-formation-rate space. The star-formation rate (SFR) is normalized to that of the ‘main sequence’³⁷ at the redshift and stellar mass of each galaxy ($\text{SFR}_{\text{MS}(z, M_*)}$). **b**, Location in stellar-mass–size space. The size is the half-light radius measured in the observed H-band corrected to the rest-frame 5,000 Å (R_e^{5000}) and normalized to that of the mass–size relation for star-forming galaxies²⁶ at the redshift and stellar mass of each source ($R_{e, \text{SFGs}(z, M_*)}^{5000}$). In **a** and **b**, the greyscale image shows the distribution of the underlying galaxy population at $0.7 < z < 2.7$ taken from the 3D-HST source catalogue at $\log(M_*/M_\odot) > 9.0$ and $K_{\text{AB}} < 23$ mag (the magnitude cut applied when selecting KMOS^{3D} targets and corresponding roughly to the completeness limits of the parent samples for SINS/zC-SINF targets). The current 2.5-year KMOS^{3D} sample is shown with blue circles, and the SINS/zC-SINF sample with green diamonds. The two KMOS^{3D} and four SINS/zC-SINF galaxies with individual outer rotation curves (RCs) are plotted as yellow circles and

diamonds, respectively. Similarly, the KMOS^{3D} and SINS/zC-SINF galaxies included in the stacked rotation curve are plotted as red circles and diamonds. All 3D-HST and KMOS^{3D} galaxies are included in **a**, whereas only star-forming galaxies (SFGs) are shown in **b**, defined as having a specific star-formation rate higher than the inverse of the Hubble time at their redshift. The galaxies with individual outer rotation curves lie on and up to a factor of four times the main-sequence (MS) in star-formation rate (with mean and median $\log(\text{SFR}/\text{SFR}_{\text{MS}}) = 0.24$), and have sizes 1.2–2 times the M_* – R_e^{5000} relation (‘M–R SFGs’; mean and median offset in $\log(R_e^{5000}) \approx 0.2$ dex). In star-formation rate and R_e^{5000} , the distribution of the stacked rotation-curve sample is essentially the same as the reference 3D-HST population in mean/median offsets (approximately 0.06 dex above the main-sequence and 0.07 dex above the mass–size relation) and in their scatter about the relationships (approximately 0.3 dex in $\log(\text{SFR})$ and 0.17 dex in $\log(R_e^{5000})$); see refs 26, 37.

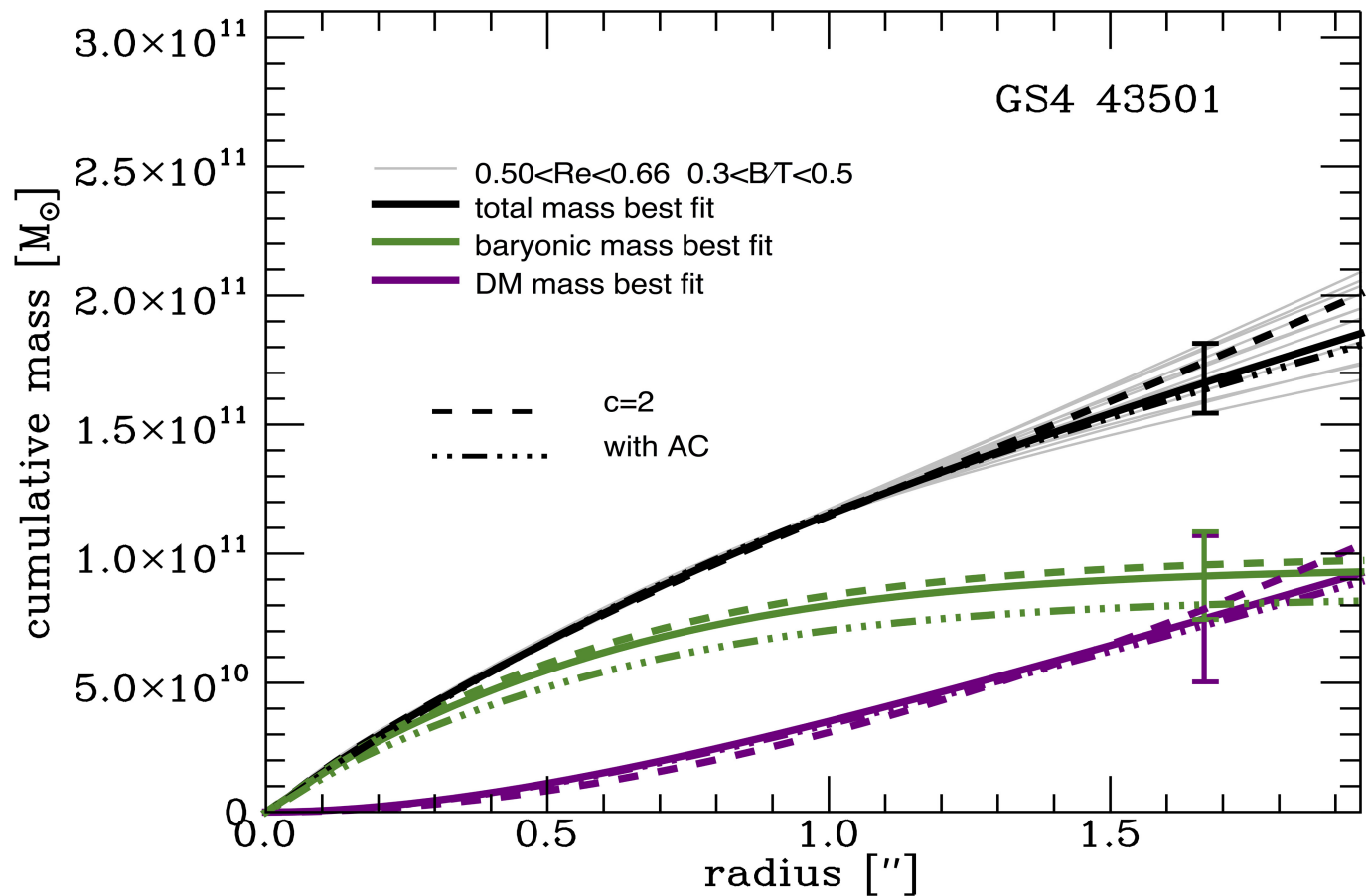


Extended Data Figure 2 | Quality of fit and error of parameter determinations. The reduced chi-squared χ^2_{reduced} as a function of the dark-matter fraction f_{DM} at $R_{1/2}$ for the six galaxies in our sample, once the other parameters (x_0 , y_0 , the position angle of the kinematic major axis PA_{maj} , i , σ_0 , $R_{1/2}$ and B/T) are fixed at their best-fit values. Global minima

are marked by circles; error bars give $\Delta\chi^2 = \pm 4$ ranges, corresponding to confidence levels of 95% (2 r.m.s.) under the assumption of single-parameter Gaussian distributions. This is the most important parameter dependence for our dataset.

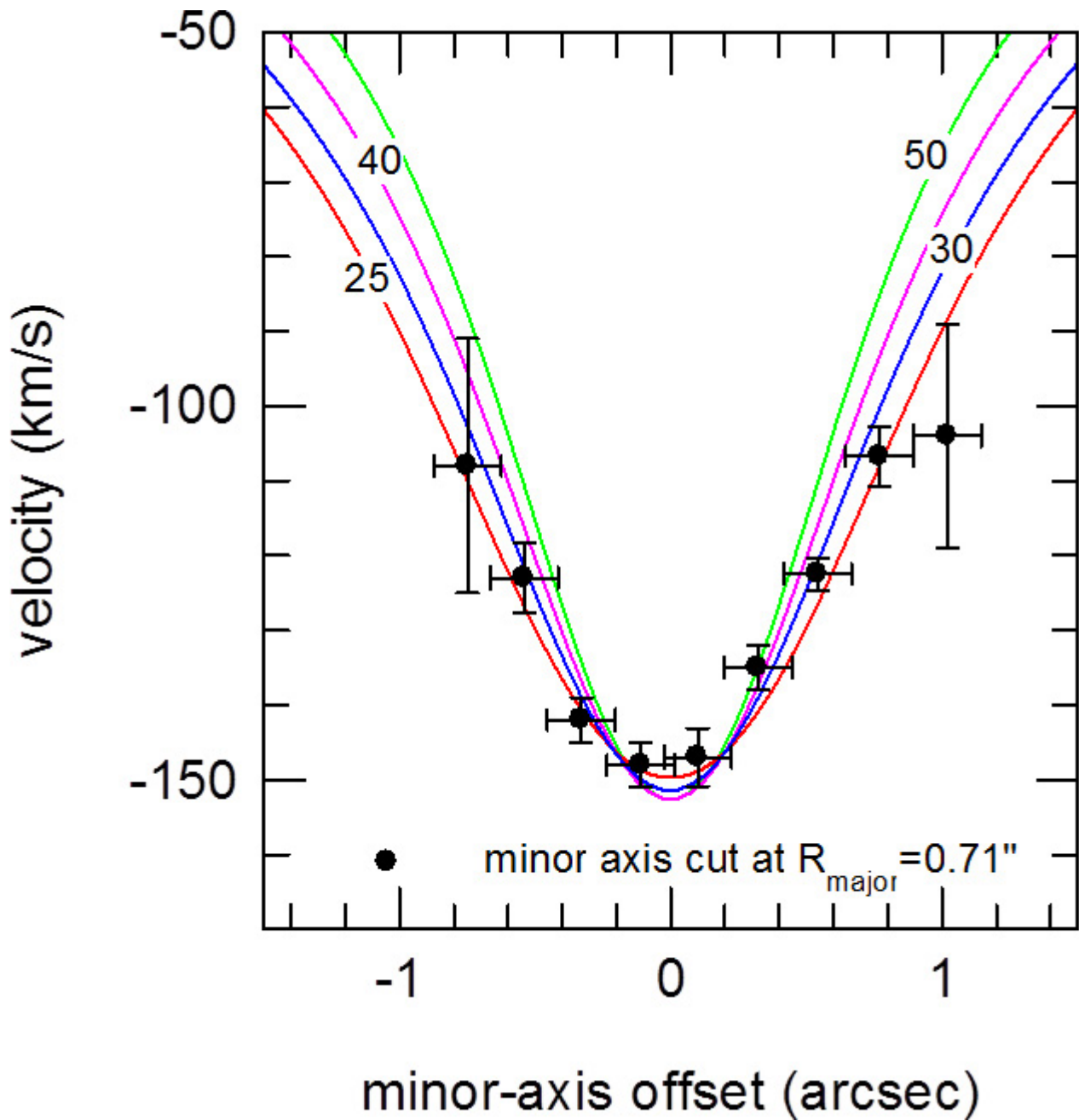


Extended Data Figure 3 | Mean changes in f_{DM} and χ_{red}^2 for changes in the secondary parameters B/T and $R_{1/2}$, for COS 01351, D3a 6397, GS4 43501 and D3a 15504. Changes in B/T and $R_{1/2}$ are labelled ' $B/T \pm 0.1$ ' and ' $R_{1/2} \pm 1\sigma$ ', respectively, where 1σ is the uncertainty on $R_{1/2}$ given in Table 1; χ_{red}^2 is the reduced chi-squared.



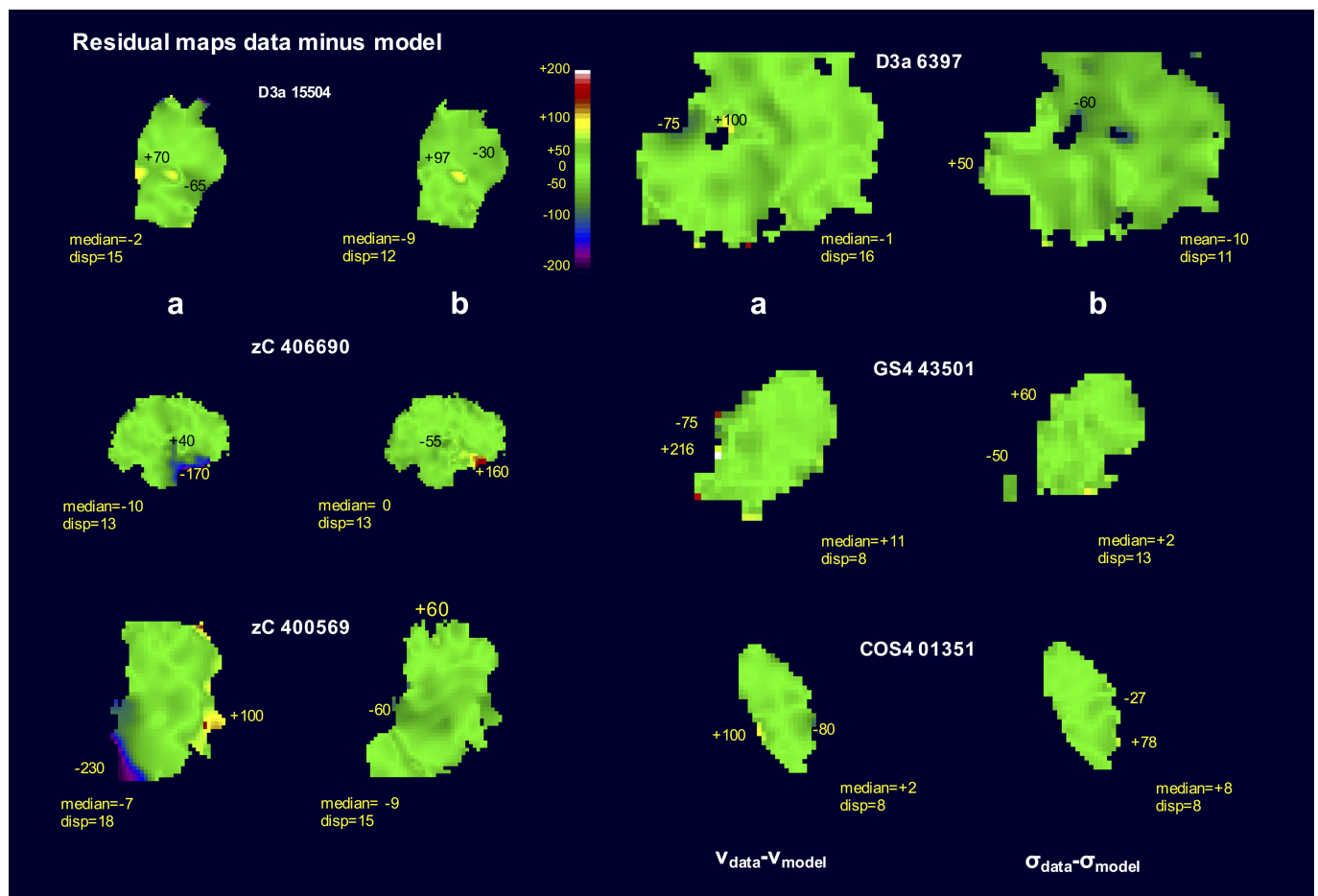
Extended Data Figure 4 | Cumulative mass as a function of radius for one of our studied galaxies (GS4 43501). Solid lines show the best fit; error bars show the variations in total (black, grey), baryonic (green) and dark-matter (DM; purple) mass at the outermost projected radius constrained by our data, if deviations from B/T and $R_{1/2}$ within the uncertainties are considered (only cases with $\chi^2_{\text{reduced}} < 1.75$ are considered). Dashed lines show the best fit for a model with lower

concentration parameter ($c = 2$ instead of $c = 5$); dashed-dotted lines show the best fit for a model with adiabatic contraction (AC)⁹⁷. Both modifications of the dark-matter profile lead to changes in the cumulative mass that are smaller than those obtained by varying B/T and $R_{1/2}$ within the above uncertainties. The grey lines encompass variations in the dark-matter fraction of $f_{\text{DM}}(R_{1/2}) = [0.14, 0.27]$ (best-fit $f_{\text{DM}}(R_{1/2}) = 0.19$).



Extended Data Figure 5 | Minor axis cut at $R_{\text{major}} = 0.71''$ of D3a 15504. Shown are the velocities (data points, with 1 r.m.s. error bars) and disk models for different inclinations (lines): 25° (red), 30° (blue), 40° (magenta) and 50° (green). The minor-axis cut favours a low inclination.

In combination with the morphology of the stellar surface density distribution (Fig. 1) and the constraint on the baryonic mass of the disk, this yields an overall inclination of $34^\circ \pm 5^\circ$ (Table 1). R_{major} is the radial distance from the centre of the galaxy along the kinematic major axis.



Extended Data Figure 6 | Residual maps. **a, b**, Residual maps (data minus model) for velocity (**a**; $v_{\text{data}} - v_{\text{model}}$) and velocity dispersion (**b**; $\sigma_{\text{data}} - \sigma_{\text{model}}$), for the six galaxies studied here. The colour scale is the same in all maps (from -200 km s^{-1} (purple) to $+200 \text{ km s}^{-1}$ (white)). Minimum and maximum values are noted in each map, as are the median and median dispersion ('disp') values.